

Research Article

Rural Masonry Isolating Structure and LRB Experiment: Seismic Resistance Properties and Statistical Data Curve Analyses

Jiayao Zheng 

Xi'an University of Finance and Economics, Xi'an, China

Correspondence should be addressed to Jiayao Zheng; 175233935@qq.com

Received 10 March 2020; Revised 13 November 2020; Accepted 10 December 2020; Published 29 December 2020

Academic Editor: Hugo C. Biscaia

Copyright © 2020 Jiayao Zheng. This is an open access article distributed under the Creative Commons Attribution License, which permits unrestricted use, distribution, and reproduction in any medium, provided the original work is properly cited.

The low masonry structure is the most commonly applied building type in rural China. It is possible to install small-diameter, low cost, and easily constructed laminated rubber bearing (LRB) components. Isolation technology has broad application prospects in rural buildings. We developed a small-diameter LRB in this study wherein the isolation layer is set above the floor for easy installation and replacement. We built and tested 4 walls to observe the effects of different LRB thicknesses; we assessed test respective phenomena and seismic parameters accordingly. We ran another test on five small-diameter LRB components with varying horizontal stiffness, different forms of shear strain-equivalent horizontal stiffness, and postyield stiffness while changing the fitting formula for the second shape coefficient to give small-diameter LRB design providing gist.

1. Introduction

The isolation structure system serves to protect structural and nonstructural components in the building in which it is installed [1]. There is an urgent demand for new research on low masonry structure seismic building technology [2]. Rural buildings rarely contain laminated rubber bearing (LRB) isolation technologies [3]. Currently available seismic isolation techniques yet merit improvement to meet today's demand for low masonry structures [4]. Previous researchers have added sliding isolated bearings [5] to rural masonry structures, but these bearings are limited to relatively few specific types of structures.

In this study, we conducted an experiment consisting of four 1/2-ratio pseudodynamic seismic tests on masonry wall structures. We used one piece of a masonry wall with no isolation bearing (SRB) and three with different LRB specifications, completing 4 groups of masonry building bearing wall models to the seismic performance test. The equivalent horizontal stiffness, postyield stiffness, and damping ratio [6] of the isolation layer and bearing were determined throughout the experiment to gather workable data for subsequent mechanical analyses. We propose a

method for the design of seismic isolation bearings accordingly [7]. The masonry wall (Figure 1(a)) was numbered "MLQT-1." The other three walls using LRB all have a diameter of 120 mm but heights of 50 mm, 70 mm, and 90 mm, respectively (Figure 1(b)), in addition to the 90 mm LRB wall. These specimens are numbered MLQT-2, MLQT-3, and MLQT-4, respectively.

The bearing wall test loading device is shown in Figure 2. According to the actual loading state of the wall, a loading device was utilized to impose a vertical uniform load as a voltage regulator was used to maintain stable axial force during the test [8]. A horizontal maximum load was applied to the top of the wall to simulate an El Centro wave peak acceleration. An electric hydraulic servo actuator [9] was used to apply different peaks of acceleration waves until the failure of the LRB or wall, respectively.

We also conducted an experiment to test various LRB mechanical parameters based on the "isolated rubber bears experimental method" [10]. Under these standards, the shear strain was 50%, 100%, and 250% corresponding to maximum displacement to calculate the LRB equivalent horizontal stiffness and damping ratio [11]. Based on the wall size of typical existing rural masonry structures, the design of experimental LRB is under 190 mm, has 12 rubber layers

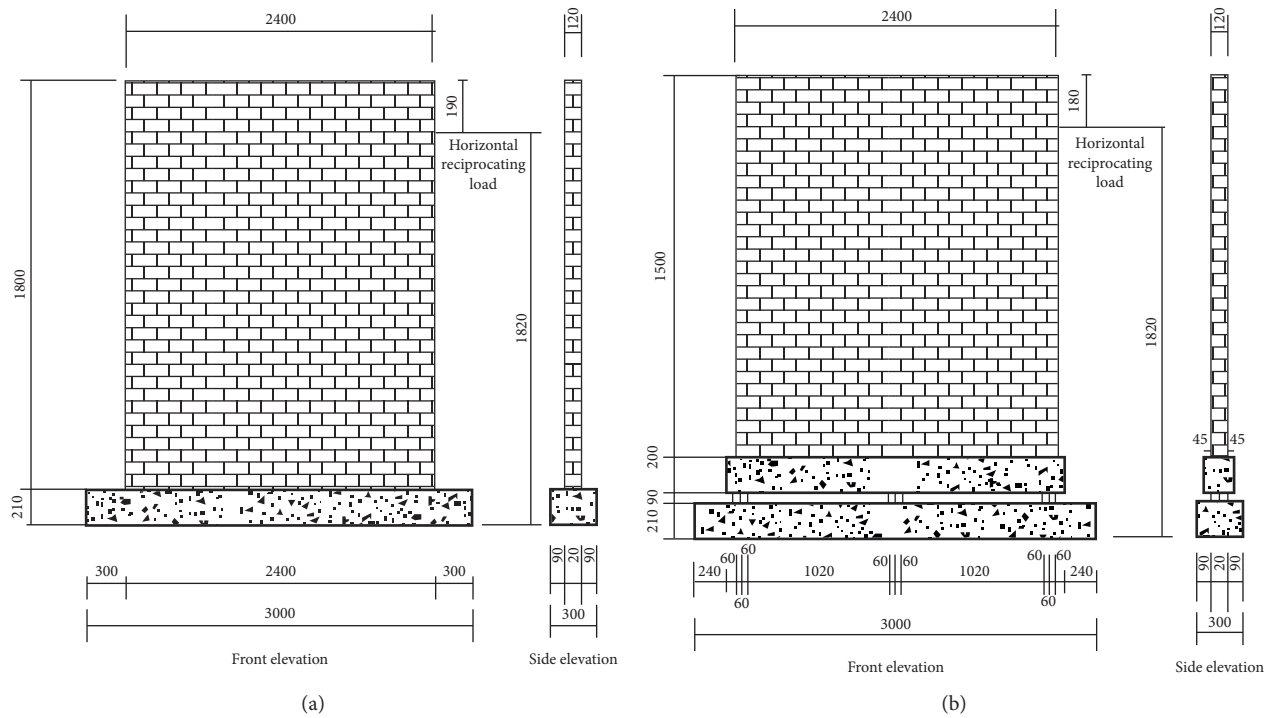


FIGURE 1: Masonry wall specimens: (a) MLQT-1; (b) MLQT-4.

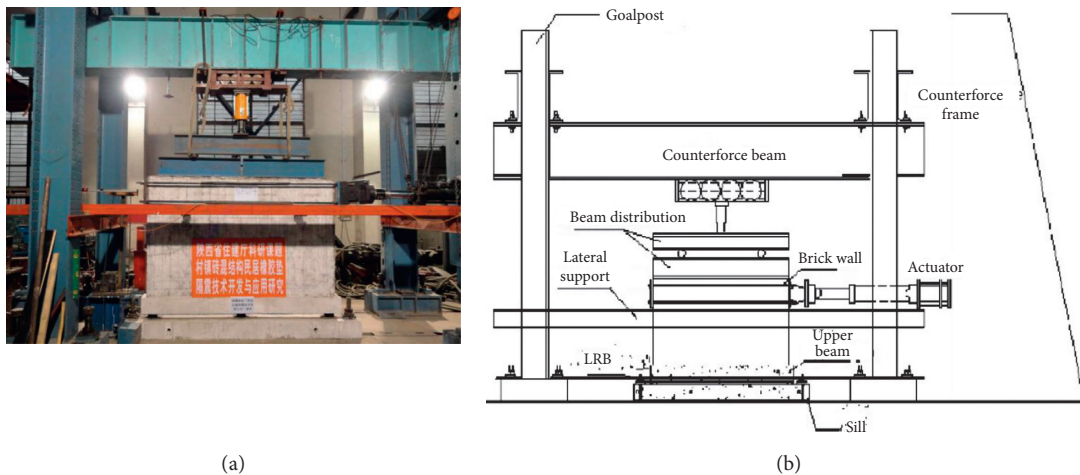


FIGURE 2: Bearing wall experiment loading device: (a) photo; (b) drawing.

each 1.8 ~ 3.5 mm thick, and has a lead core of approximately 12 mm in diameter. We used five isolated bars all with an external diameter of 120 mm as lead core laminated rubber supports. The LRB is composed of a cover steel plate, thin steel plate, layer rubber, and lead core; all are cylindrical in shape. The LRB structure and specifications are listed in Table 1. Each type of LRB was tested in two replications.

We conducted the horizontal stiffness experiment on these LRB specimens at the Guangzhou University Engineering Seismic Research Center on a 1000 t electro-hydraulic servo press and shear tester with the horizontal dynamic loading equipment shown in Figure 3. The experiment horizontal loading was controlled by maximum

displacement [12]. The vertical loading was 30 kN as the same type of two LRB specimens was inputting 0.1 Hz and 0.5 Hz sine waves separately with different values of peak acceleration in the horizontal direction. The maximum displacement changed as the shearing strain was set to 50%, 100%, and 250% [13]. Loading was recycled four times and the third hysteresis loop was calculated [14], where the LRB number end-term represents the sine wave frequency as GZ1-0.1 GZ1-0.5.

We conducted five small-diameter LRB horizontal stiffness tests to observe the effects of different LRB horizontal shear strains and second shape coefficients [15] with different forms of equivalent horizontal stiffness, postyield

TABLE 1: Experimental bar specifications.

Bar model	Rubber shear elasticity modulus (MPa)	Effective diameter (mm)	Number of layers	Rubber layer thickness (mm)	Thin steel plate thickness (mm)	Thin steel plate number	Lead core diameter (mm)	Cover steel plate thickness (mm)	Bear overall height (mm)	Second shape coefficient = dia/total thickness of the rubber layer
GZ1	0.39	110	12	1.8	2	11	12	10	63.6	5.1
GZ2	0.39	110	12	2.5	2	11	13	10	72	3.7
GZ3	0.39	110	10	3.5	2	9	14	10	73	3.1
GZ4	0.39	110	12	1.9	2	11	10	10	64.8	4.8
GZ5	0.55	110	12	1.8	2	11	12	10	63.6	5.1

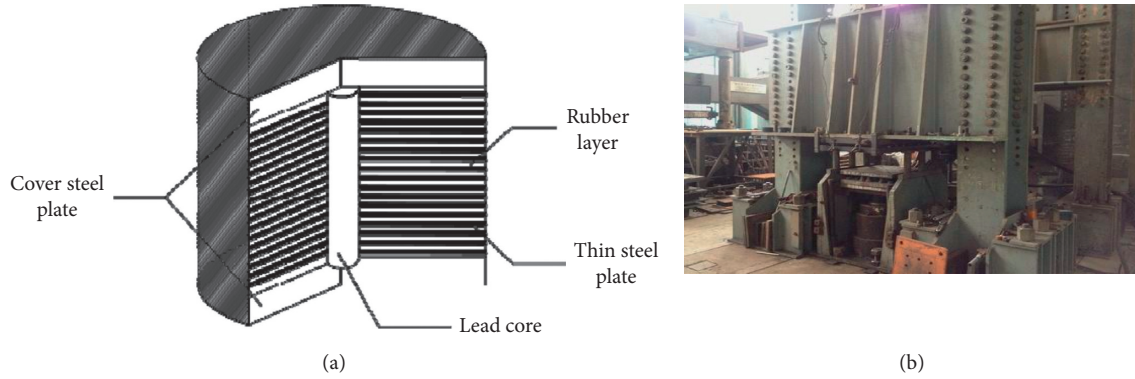


FIGURE 3: Testing LRB and equipment: (a) dynamic loading equipment; (b) LRB.

stiffness, and hysteretic behavior-related mechanical properties [16]. We wrote a fitting formula for changes in shear strains with equivalent horizontal stiffness, postyield stiffness, and second shape coefficient. We also analyzed the relationship between the structural mode damping coefficient and horizontal displacement; this formed a correlation curve.

The small-diameter LRB mechanical property parameters for rural dwellings provided a reference for our LRB test specimen design. The horizontal isolation layer increases the fundamental horizontal period of the structure significantly; this layer is what isolates the structural system from strong seismic disturbances in the ground. Structural deformation is concentrated in the isolation layer [17], so the LRB should be designed according to predetermined seismic aims and applicable targets to function properly.

2. Working Principles of Masonry Wall Experiment and LRB Design

2.1. Simulating El Centro Seismic Waves. We adopted pseudodynamic loading conditions for the purposes of this test. A horizontal simulating was applied to the top of the wall [18] with an El Centro seismic wave. The vertical load was applied to simulate the actual loading state of the wall through the vertical device, the dynamic load acceleration, the force of inertia, and the velocity damping force. The displacement of the elastic restoring force can be expressed as follows:

$$R_{IF}(d, v, a) + R_{SS}(d, v, a) = F, \quad (1)$$

where R_{IF} is the isolation layer counterforce, R_{SS} is the superstructure counterforce, F is the external load, and $d, v,$ and a are displacement, velocity, and acceleration, respectively. The constant equation of motion [19] is

$$Ma_i + Cv_i + Kd_i = F. \quad (2)$$

The following assumption [20] was imposed for the i step velocity and acceleration:

$$v_i = \frac{d_{i+1} - d_{i-1}}{2\Delta t}, \quad (3)$$

$$a_i = \frac{d_{i+1} - 2d_i + d_{i-1}}{\Delta t^2}, \quad (4)$$

where $M, C,$ and K are the mass, damping, and stiffness matrix, respectively. The $i + 1$ step displacement expression can be written by integrating equations (2)–(4).

2.2. LRB Design

2.2.1. Shinnev et al.'s Method. The superstructure was fitted here with the LRB and considered as a rigid body. Displacement on one side moves along a similar trapezoid (first mode) as the oscillating displacement increases in equal proportion at the same height. The double bilinear isolation system can be simplified using this model [21]. The effective nature period of vibration can be determined via

$$T_B = 2\pi\sqrt{\frac{M}{K_B}}, \quad (5)$$

$$\xi_B = \xi_b + \xi_h, \quad (6)$$

$$T_b = \frac{C_b T_B}{4\pi M}, \quad (7)$$

$$\xi_h = \left(\frac{2}{\pi}\right) \frac{A_h}{4S_b X_b}, \quad (8)$$

where ξ_b is the effective velocity damping coefficient, K_B is the secant stiffness of the LRB, A_h is the hysteretic curve area, and S_b and X_b represent the effective restoring force and displacement.

The equivalent seismic response in the bilinear [22] isolation system can be derived from the response spectrum of the earthquake, per the given seismic design:

$$X_b \approx C_F S_D(T_B, \xi_B) S_b \approx Q_y + K_{b2}(X_b - X_y), \quad (9)$$

where Q_y is the yield force and K_{b2} is the second stiffness.

2.2.2. AMER UBC Section Method. Assuming that seismic shear force [23] is discontinuous in the isolation system. Its isolated interface base shear formula is

$$V_b = \frac{k_{\max} D}{1.5}, \quad (10)$$

and the superstructure base shear formula is

$$V_B = \frac{k_{\max} D}{R_{w1}},$$

$$D = \frac{10ZNS_1 T_1}{B}, \quad (11)$$

$$T_1 = 2\pi\sqrt{\frac{W}{K_{\min} g}},$$

where K_{\max} is the maximum effective stiffness, R_{w1} is a ductility coefficient of the superstructure, and Z is the zone coefficient. B is a coefficient associated with material damping, N is a coefficient associated with the structure and the active fracture distance, S_1 is the ground influence coefficient, W is the total weight of the structure above isolation interface, and K_{\min} is the isolated system minimum effective stiffness.

The superstructure seismic force distribution is rectangular along its height when the base is isolated:

$$F_i = \frac{V_B W_i}{\sum_{i=1}^n W_i}, \quad (12)$$

$$K_{\text{eff}} = \frac{F^+ - F^-}{\Delta^+ - \Delta^-},$$

where W_i is the floor variate, n is the number of layers, K_{eff} is the equivalent stiffness, and F^- and Δ^- are the minimum force/displacement in one cycle.

2.2.3. Zhou Method. The superstructure is equivalent to a particle, as is the isolated layer [24]. The equivalent mass of the superstructure can be obtained when the two systems' kinetic energy and base shear are considered to be equal.

$$M_{s,\text{eq}} = \frac{\left[\sum_{i=1}^N m_i x_i(i)\right]^2}{\sum_{i=1}^N m_i x_i^2(i)}. \quad (13)$$

The equivalent stiffness is

$$K_{s,\text{eq}} = \left[\frac{\sum_{i=1}^N M_i x_i(i)}{\sum_{i=1}^N m_i x_i^2(i)}\right]^2 \sum_{i=1}^N k_i x_i^2(i), \quad (14)$$

where N is the number of layers, m_i is the layer I mass, k_i is the layer I stiffness, and $x_1(i)$ is a fixed base fundamental mode.

The period is

$$T_l \approx \sqrt{T_{s,l}^2 + T_b^2},$$

$$T_2 = T_{s,l} \sqrt{\left(1 + \mu\right) \left(1 + \frac{T_{s,l}^2}{T_b^2}\right)}, \quad (15)$$

$$T_{s,l} = 2\pi\sqrt{\frac{M_{s,\text{eq}}}{K_{s,\text{eq}}}}.$$

The first model participation coefficient is

$$\frac{x_s}{x_b} = 1 + \frac{T_{s,1}^2}{T_b^2} \gamma_1 = \frac{1 + \mu(1 + T_{s,1}^2)}{1 + \mu(1 + 2(T_{s,1}^2/T_b^2))}, \quad (16)$$

and the second model participation coefficient [25] is

$$\frac{x_s}{x_s} \approx -[\mu + (1 + \mu)] \frac{T_{s,1}^2}{T_b^2} \gamma_2 = \frac{T_{s,1}^2}{T_b^2} \frac{1}{\mu(1 + 2(T_{s,1}^2/T_b^2))}, \quad (17)$$

where $\mu = M_{s,\text{eq}}/M_b$ is the mass ratio, $T_b = 2\pi\sqrt{(M_b + M_{s,\text{eq}}/K_b)}$ is the hypothetical superstructure rigid body isolated structure period, M_b is the mass of the isolated layer, and K_b is the stiffness of the isolated layer.

2.2.4. Proposed Method. We calculated the horizontal equivalent stiffness and equivalent viscous damping ratio in the isolated layer using an oscillation equation's plural damping theory. The natural vibration period of a rural masonry structure is short, so the appropriate horizontal damping coefficient is 1.2 [25]. A simplified calculation gets the isolation layer horizontal stiffness and equivalent damping ration:

$$\begin{aligned} K_h &= nK_j, \\ \zeta_{eq} &= \zeta_j, \end{aligned} \quad (18)$$

where K_h is the isolated layer's horizontal equivalent stiffness, K_j is each signal's LRB horizontal equivalent stiffness, ζ_{eq} is the isolated layer's equivalent viscous damping ratio, ζ_j is the LRB's equivalent viscous damping ratio, and n is the number of bearings.

The horizontal direction seismic reduction coefficient is expressed as

$$\beta = 1.2\eta_2 \left(\frac{T_g}{T_1} \right)^\gamma, \quad (19)$$

where β is the horizontal seismic reduction coefficient, η_2 is the damping adjustment coefficient, γ is the curve descending section attenuation coefficient, T_g is the Eigen period, and T_1 is the isolated structure essential nature period of vibration.

$$\begin{aligned} \eta_2 &= 1 + \frac{0.05 - \xi_{eq}}{0.08 + 1.6\xi_{eq}}, \\ \gamma &= 0.9 + \frac{0.05 - \xi_{eq}}{0.3 + 6\xi_{eq}}, \\ T_1 &= 2\pi \sqrt{\frac{G}{K_h g}}. \end{aligned} \quad (20)$$

The LRB horizontal displacement under strong seismic conditions can be calculated as follows:

$$\mu_i \leq [\mu_i], \quad (21)$$

where μ_i is the LRB's horizontal displacement under strong seismic conditions; $[\mu_i]$ is the limit of displacement when the LRB effective diameter is multiplied by less than 0.55 and the inner rubber total thickness is multiplied threefold [26].

$$\mu_e = \frac{\lambda_s \alpha_h G}{K_h}, \quad (22)$$

$$\mu_i = 1.15\mu_e,$$

where μ_e is the isolation layer centroid of horizontal displacement in a "rare occurrence" earthquake scenario and λ_s is the near field coefficient.

2.3. LRB Mechanical Model

2.3.1. Equivalent Linear Model. We used a linear stiffness and damping equivalent calculation method to assess LRB mechanical properties. The linear stiffness is secant in this case:

$$F = k\mu. \quad (23)$$

We analyzed the LRB damping force separately according to a unidirectional damping resilience-displacement relation:

$$F = c\dot{\mu}, \quad (24)$$

$$\xi = \frac{W_d}{4\pi W_e} = \frac{W_d}{2\pi k\mu^2}, \quad (25)$$

where ξ is the equivalent stiction damping ratio, W_d is the equivalent damping energy consumption area, W_e is the elastic resilience work area, k is the horizontal equivalent linear stiffness, F is the LRB's horizontal resilience, and μ is the LRB's horizontal displacement.

Plugging the formulas (23) and (25) to (24), we get the following formula:

$$c = \frac{4\pi P\xi}{Tg}, \quad (26)$$

where c is the equivalent stiction damping ratio, P is the LRB's vertical loads, T is the isolated structure's first natural period of vibration, and g is the gravitational acceleration.

The linear elastic unit [27] comprised of stiffness (K_x, K_y, K_r), combination stiffness center (x_K, y_K) related to the isolation layer centroid (x_B, y_B), and stiffness eccentricity [28] is $e_x^B = x_K - x_B, e_y^B = y_K - y_B$.

$$\begin{cases} F_x = \sum_i k_{ix} (\mu_x^B - e_y^B \mu_r^B), \\ F_y = \sum_i k_{iy} (\mu_y^B - e_x^B \mu_r^B), \\ T = \sum_i (k_{ix} y_i^2 + k_{iy} x_i^2) \mu_r^B + \sum_i k_{iy} e_x^B e_y^B - \sum_i k_{ix} e_y^B e_x^B, \end{cases} \quad (27)$$

where k_{ix}, k_{iy}, x_i^2 , and y_i^2 represent the i -th LRB's x - and y -direction shear stiffness and coordinates, respectively.

$$\begin{cases} F_x = C_x (\dot{\mu}_x^B - e_y^B \dot{\mu}_r^B), \\ F_y = C_y (\dot{\mu}_y^B - e_x^B \dot{\mu}_r^B), \\ T = C_r \dot{\mu}_r^B + C_y e_x^B \dot{\mu}_y^B - C_x e_y^B \dot{\mu}_x^B. \end{cases} \quad (28)$$

2.3.2. Double Linear Model. There are three main types of the double linear model: the ideal elastic-plastic model, linear strengthen elastic-plastic model, and negative stiffness property elastic-plastic model [29]. We used the linear strengthen elastic-plastic model to unify force-displacement under analysis in this study.

$$\begin{cases} F_b = K_e \mu_b, & \mu_b < \mu_y, \\ F_b = \alpha K_e \mu_b + (1 - \alpha) F_y, & \mu_b > \mu_y, \end{cases} \quad (29)$$

where α is the ratio of postyield stiffness to preyield stiffness, F_y is the yield force, μ_y is the yield displacement, K_e is the preyield stiffness, F_b is LRB resilience, and μ_b is LRB displacement.

We took the double linear model property LRB for equivalent linear model simulation. The equivalent stiffness and equivalent stiction damping ratio in this case is

$$K_{\text{eff}} = \frac{F_b}{\mu_b},$$

$$\xi_{\text{eff}} = \frac{2}{\pi} (1 - \alpha) \left(\frac{\mu_b - \mu_y}{\mu_b} \right) \frac{F_y}{F_b}. \quad (30)$$

We assessed the LRB equivalent stiffness and equivalent stiction damping ratio under different horizontal displacement conditions. The double linear model force parameter conversion formula is

$$\left\{ \begin{array}{l} Q_y = \frac{F_{b1}\mu_{b2} - F_{b2}\mu_{b1}}{\mu_{b2} - \mu_{b1}}, \\ K_p = \frac{F_{b2} - F_{b1}}{\mu_{b2} - \mu_{b1}}, \\ \mu_y = \frac{F_{b2}\mu_{b2}\xi_{b2}\mu_{b1} - F_{b1}\mu_{b1}\xi_{b1}\mu_{b2}}{F_{b2}\mu_{b2}\xi_{b2} - F_{b1}\mu_{b1}\xi_{b1}}, \\ F_y = \frac{F_{b1}F_{b2}(\mu_{b2}\xi_{b2} - \mu_{b1}\xi_{b1})}{F_{b2}\mu_{b2}\xi_{b2} - F_{b1}\mu_{b1}\xi_{b1}}, \\ K_e = \frac{F_{b1}F_{b2}(\mu_{b2}\xi_{b2} - \mu_{b1}\xi_{b1})}{F_{b2}\mu_{b2}\xi_{b2}\mu_{b1} - F_{b1}\mu_{b1}\xi_{b1}\mu_{b2}}, \end{array} \right. \quad (31)$$

where $(F_{b1}, \mu_{b1}, K_{b1}, \xi_{b1})$, $(F_{b2}, \mu_{b2}, K_{b2}, \xi_{b2})$ reveal various displacement levels of LRB equivalent stiffness and equivalent stiction damping ratios. $\xi_{b1} - (F_{b1}, \mu_{b1})$, $\xi_{b2} - (F_{b2}, \mu_{b2})$ represent the equivalent stiction damping ratio.

The LRB surface was modeled here using a Prager mobile induration model [30]. We hypothesized that a_x, a_y are the x, y -direction ratio of postyield shear stiffness and preyield shear stiffness, and that F_x^y, Y_x, F_y^y , and Y_y are the x, y -direction uniaxial load yielding strength and displacement. The yield surface function is

$$S = \left(\frac{|F_x - F_x^0|}{F_x^y} \right)^n + \left(\frac{|F_y - F_y^0|}{F_y^y} \right)^n - 1 = 0, \quad (32)$$

where S is the yield function, F_x^0, F_y^0 are the x, y -direction loading yield surface center of inertia, and n is the loading yield surface curve exponent.

The yield center mobile increases as follows:

$$\begin{aligned} \begin{pmatrix} dF_x^0 \\ dF_y^0 \end{pmatrix} &= \frac{1}{\left((F_x - F_x^0)/F_x^y \right)^2 + \left((F_y - F_y^0)/F_y^y \right)^2} \begin{pmatrix} \left(\frac{F_x - F_x^0}{F_x^y} \right)^2 & \frac{(F_x - F_x^0)(F_y - F_y^0)}{(F_y^y)^2} \\ \frac{(F_x - F_x^0)(F_y - F_y^0)}{(F_x^y)^2} & \left(\frac{F_y - F_y^0}{F_y^y} \right)^2 \end{pmatrix} \begin{pmatrix} dF_x \\ dF_y \end{pmatrix} \\ &= \begin{pmatrix} \left(\frac{F_x - F_x^0}{F_x^y} \right)^2 & \frac{(F_x - F_x^0)(F_y - F_y^0)}{(F_y^y)^2} \\ \frac{(F_x - F_x^0)(F_y - F_y^0)}{(F_x^y)^2} & \left(\frac{F_y - F_y^0}{F_y^y} \right)^2 \end{pmatrix} \begin{pmatrix} dF_x \\ dF_y \end{pmatrix}, \end{aligned} \quad (33)$$

and the circle yield surface [31] is expressed as

$$\begin{pmatrix} du_x \\ du_y \end{pmatrix} = \left(\begin{pmatrix} K_{ex} \\ K_{ey} \end{pmatrix} \right)^{-1} + \frac{1}{(\alpha_x/(1-\alpha_x))K_{ex}((F_x - F_x^0)/(F_x^y)^2) + (\alpha_y/(1-\alpha_y))K_{ey}((F_y - F_y^0)/(F_y^y)^2)} \cdot \begin{pmatrix} \left(\frac{F_x - F_x^0}{(F_x^y)^2} \right)^2 & \left(\frac{F_x - F_x^0}{(F_x^y)^2} \right) \left(\frac{F_y - F_y^0}{(F_y^y)^2} \right) \\ \left(\frac{F_y - F_y^0}{(F_y^y)^2} \right) \left(\frac{F_x - F_x^0}{(F_x^y)^2} \right) & \left(\frac{F_y - F_y^0}{(F_y^y)^2} \right)^2 \end{pmatrix} \begin{pmatrix} dF_x \\ dF_y \end{pmatrix}, \quad (34)$$

$$\frac{F_x - F_x^0}{(F_x^y)^2} K_{ex} d\mu_x + \frac{F_y - F_y^0}{(F_y^y)^2} K_{ey} d\mu_y \begin{cases} > 0, & \text{loading,} \\ = 0, & \text{neutral,} \\ < 0, & \text{unload.} \end{cases}$$

2.3.3. *Triple Linear Model.* A triple linear model can be adopted upon extensive deformation in the structure (i.e.,

stiffness hardening). The resilience-displacement relationship [32] in this case is

$$F = \begin{cases} K_1 \mu, & \mu \leq D_1, \\ K_1 \mu + (K_2 - K_1)(\mu - D_1), & D_1 < \mu \leq D_2, \\ K_1 \mu + (K_2 - K_1)(\mu - D_1) + (K_3 - K_2)(\mu - D_2), & \mu > D_2, \end{cases} \quad (35)$$

where F is resilience, K_1 is the shear stiffness when $\mu \leq D_1$, K_2 is the shear stiffness when $D_1 < \mu \leq D_2$, K_3 is the shear stiffness when $\mu > D_2$, and μ is the displacement.

The stiction damping model [33] is

$$F_D = \left(\sum_{i=1}^n [F_{0i} + C_i |\dot{\mu}|^{\rho_i}] \right) \text{sgn}(\dot{\mu}), \quad (36)$$

where F_{0i} is 0 velocity damping, C_i is the damping coefficient, and ρ_i is a damping exponential. Coulomb damping $\rho_i = 0$, linear ratio damping $\rho_i = 1$, and nonlinear damping ρ_i varies.

The force-displacement relation [34] is

$$F_D = C_i \text{sgn}(\dot{\mu}) F_D = C_i |\dot{\mu}| \text{sgn}(\dot{\mu}) F_D = C_i |\dot{\mu}|^2 \text{sgn}(\dot{\mu}). \quad (37)$$

Our model is a combination of double and triple linear models, wherein we consider five LRB equivalent damping ratios with a total damping ratio of 10 ~ 20% and a high damping ratio of 15 ~ 20% shown in Table 2. We observed a 250% hysteretic curve shape shown in Figure 4(b) that emerged on both sides of the curve and degenerated as displacement resilience increased.

3. Wall Experiment and Seismic Behavior

3.1. *Relevant Phenomena.* Our specimen MLQT-1 is an uninstalled LRB wall. The corresponding relation between earthquake intensity and peak acceleration of seismic waves

was imposed under 70, 100, 300, and 400 gal El Centro wave excitation models. We found no obvious cracks until reaching displacement of 9.6 mm and horizontal force of +137.879 kN, at which point the corresponding peak acceleration of seismic waves was 300 gal. We continued reverse loading until finding oblique cracks in the wall as shown in Figure 5; these shear cracks developed in the wall during pushing and pulling in a typical "X" shape [35], at which point the wall presented shear failure.

MLQT-2 was equipped with a 50 mm LRB masonry specimen and input with a damping ratio of 0.15 and 70, 100, 300, 400, and 510 gal El Centro wave excitation models [36]. We calculated the LRB's ultimate displacement according to the upper and lower beam relative displacement. When the acceleration peak reached 300 gal, the maximum displacement was 13.6 mm (exceeding LRB allowable limit of displacement 10.8 mm). The middle of the LRB was broken when the acceleration peak reached 510 gal; the wall was not damaged until the test was stopped, as shown in Figure 6.

As shown in Figure 6, MLQT-2 does not meet the design standard though the LRB and upper structure were not broken in the test. LRB thickness variations, in this case, were -1 mm, -2 mm, and -1 mm, which indicate that the wall was not compressed by the vertical load.

Specimen MLQT-3 was equipped with a 57 mm LRB masonry specimen designed to be resistant to seismic waves of 400 gal peak acceleration. Once the peak acceleration reached 400 gal, the maximum displacement was 14.2 mm, i.e., below the allowable limit of 22.5 mm. The contact

TABLE 2: LRB horizontal stiffness calculation results.

Bearing number	GZ1-0.5	GZ2-0.5	GZ3-0.5	GZ4-0.5	GZ5-0.5
Equivalent horizontal stiffness (N/mm)	278.47	177.12	156.13	211.73	328.51
Equivalent damping ratio (%)	10.6	17.25	19.24	19.07	12.52
Postyield stiffness (N/mm)	236	140	205	156	270
Yield stress	945	1160	1390	1420	1280

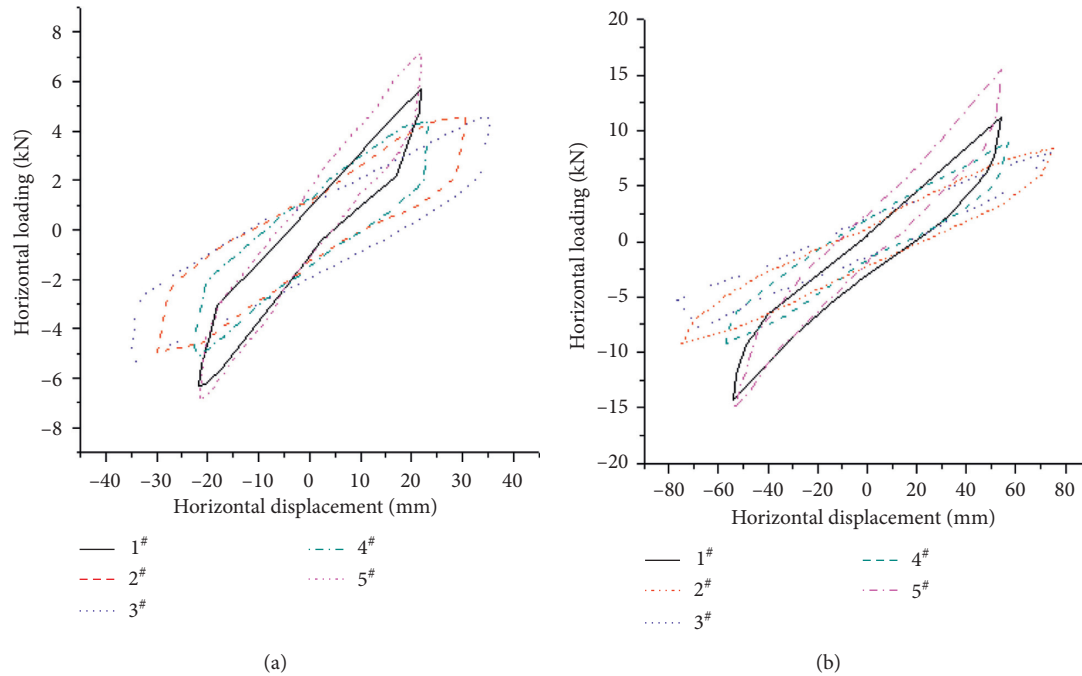


FIGURE 4: Supporter third hysteretic data: (a) 100% shear strain hysteretic loop; (b) 250% shear strain hysteretic loop.



FIGURE 5: MLQT-1 collapse state.

between the LRB and steel plate separated only slightly, which did not affect the continuation of the experiment. The maximum displacement was observed upon reaching 620 gal, at 26.4 mm, which does exceed the allowable limit. The specimen was considered to be broken at this time. The LRB internal steel plate was broken and fully exposed upon reaching 800 gal (Figure 7), though the wall did not crack by the end of the experiment.

MLQT-4 was equipped with a 90 mm LRB masonry specimen and designed to resist the peak acceleration of an 800 gal seismic wave [37]. The maximum displacement reached 39.1 mm at the peak acceleration of 800 gal, which is below the allowable limit of 60.5 mm; thus, this

specimen met the predesign specifications. Upon reaching 1,240 gal, the maximum displacement was 65.7 mm (exceeding the allowable limit of 60.5 mm) and the specimen was considered to be broken (Figure 8). Upon reaching 1,400 gal, the maximum displacement of the model structure was 76.9 mm (push), the maximum base shear was 17 kN (push), the LRB was broken, and the wall showed no cracks.

As shown in Figure 8, the MLQT-4 LRB thickness variations after the vertical loads were applied were -1 mm, -1 mm, and -2 mm. The maximum values of the additional loads were, respectively, 187.3 kN and 184.5 kN. This difference is in the allowable range and the wall was not compressed.

3.2. Data Operating of Maximum Displacement and Shear. We found that MLQT-1 280–400 gal showed a maximum displacement difference of -3 mm by -4 minus -1 mm, -7 minus -4 mm; the value changed suddenly and dramatically by the end of the test and diagonal cracks appeared through the wall. MLQT-2 reached a maximum displacement exceeding the allowable limit at 300 gal, as listed in Table 3.

The MLQT-3 allowable displacement is 22.5 mm [38], which was exceeded at 620 gal. The MLQT-4 allowable displacement is 60.05 mm, which was exceeded at 1,240 gal (Table 4).



FIGURE 6: MLQT-2: (a) LRB limit of displacement state; (b) LRB broken state.



FIGURE 7: MLQT-3: (a) LRB limit of displacement state; (b) LRB broken state.



FIGURE 8: MLQT-4: (a) LRB limit of displacement state; (b) LRB broken state.

TABLE 3: MLQT-1\MLQT-2 displacement.

Specimen number	Peak acceleration (gal)	Maximum displacement (mm)
<i>MLQT-1</i>	140	-1.879
	200	-4.280
	280	-7.251
	400	8.779
<i>MLQT-2</i>	200	9.990
	300	13.610
	400	16.657
	510	21.497

TABLE 4: MLQT-3\MLQT-4 displacement.

Specimen number	Peak acceleration (gal)	Maximum displacement
MLQT-3	400	14.231 mm (allowable disp 22.50 mm) 26.421 mm
	620	
	800	
MLQT-4	1000	50.943 mm (allowable disp 60.05 mm) 65.780 mm
	1240	
	1400	

MLQT-1, from 35 to 70 gal, applied acceleration increase of 100%, and then max base shear increased by 130%. For an increased acceleration of 40%, from 70 to 100 gal, the max base shear increased by 34% (Table 5). From 100 to 140 gal, acceleration increased by 40%, and max base shear increased by 40%. From 140 to 200 gal, acceleration increased by 40%, and max base shear increased by 70%. From 200 to 280 gal, acceleration increased by 40%, and max base shear increased by 16.8%. From 280 to 400 gal, acceleration increased by 40%, and max base shear increased by 13.7%. As shown in Table 6, the numerical percentages varied each time the peak acceleration increased by 40% [39]; the corresponding base shear percentage increased, on the whole, until the 200–280 gal range at which point it appears to decrease. In effect, the wall was in an elastic state before this acceleration and then entered the elastic-plastic stage until it broke. These numerical values are consistent with the experimental phenomena we observed.

MLQT-2, at 70 to 100 gal, increased in applied acceleration by 40%, and max base shear increased by 37.04%. From 100 to 200 gal, acceleration increased by 50%, and max shear increased by 117.40%. From 200 to 300 gal, acceleration increased by 50%, and max shear increased by 59.36%. From 300 to 400 gal, acceleration increased by 30%, and max shear increased by 30.94%. From 400 to 510 gal, acceleration increased by 26%, and max shear increased by 35.82%. The numerical percentage variations are listed in Table 6. We found that the LRB did not work before 200 gal and did work from 200 to 510 gal, and that its performance degraded from 400 to 510 gal.

MLQT-3, from 100 to 200 gal, increased in applied acceleration by 50% [40] and max base shear increased by 40%. From 200 to 280 gal, acceleration increased by 40%, and max shear increased by 20%. From 280 to 400 gal, acceleration increased by 140%, and max shear increased by 36%. From 400 to 620 gal, acceleration increased by 50%, and max shear increased by 70%. From 620 to 800 gal, acceleration increased by 30%, and max shear increased by 10%. The numerical percentage variations are listed in Table 7. It appears that the LRB performed effective isolation from 100 to 400 gal and 200 to 400 gal, but this performance was unstable after 400 gal.

MLQT-4, from 70 to 140 gal, increased in applied acceleration by 100% and in max base shear by 50%. From 140 to 200 gal, acceleration increased by 40%, and max base shear increased by 30%. From 200 to 280 gal, acceleration increased by 40%, and max base shear increased by 75%. From 280 to 400 gal, acceleration increased by 40%, and max

TABLE 5: Maximum shear with peak acceleration (MLQT-1).

Specimen number	Peak acceleration (gal)	Max base shear (kN)
MLQT-1	35	13.49
	70	-31.149
	100	-41.830
	140	-58.136
	200	-98.837
	280	115.429
	400	-131.231

base shear increased by 10%. From 620 to 800 gal, acceleration increased by 30%, and max base shear increased by 20%. From 800 to 1,000 gal, acceleration increased by 25%, and max base shear increased by 10%. From 1,000 to 1,024 gal, acceleration increased by 20%, and max base shear increased by 10%. From 1,240 to 1,400 gal, acceleration increased by 13%, and max base shear increased by 3%. The numerical percentage variations are listed in Table 8. The LRB was either not working or had unstable performance before 280 gal; its performance was stable from 620 to 1,024 gal. The LRB showed optimal isolation performance once it started working and the specimen was on the brink of destruction.

3.3. Seismic Behavior

3.3.1. Hysteretic Curve. We drew a hysteretic curve under the action of various earthquake intensities according to the test data presented above [41]. We used the MLQT-3 MLQT-4 corresponding to peak acceleration under simulated earthquake action as an example. The hysteretic curve characteristics of the bearing walls with different shape coefficients S1 and S2 [42] were compared to assess seismic absorption and isolation performance of two types of LRB wall. The hysteretic curve and hysteretic loop area of MLQT-4 under 800 gal are shown in Figure 9.

Upon reaching the yield load, MLQT-1 displacement growth accelerated though the hysteretic curve continued to present an inverse S shape. The load applied in the opposite direction decreased the wall's stiffness due to the slip effect and yet-unclosed fractures [43]. Prior to fracture closure, the specimen had relatively low stiffness with cracked reinforcement, an uncracked block, and stressed concrete. Once the damaged wall came under pressure during the loading process, the deformation velocity decreased and the wall stiffness was enhanced.

TABLE 6: Maximum shear with peak acceleration (MLQT-2).

Specimen number	Peak acceleration (gal)	Max base shear
MLQT-2	70	11.677
	100	16.006
	200	34.855
	300	55.546
	400	72.753
	510	98.816

TABLE 7: Maximum shear with peak acceleration (MLQT-3).

Specimen number	Peak acceleration (gal)	Max base shear
MLQT-3	100	9.791
	200	14.097
	280	17.660
	400	24.073
	620	40.825
	800	44.778

TABLE 8: Maximum shear with peak acceleration (MLQT-4).

Specimen number	Peak acceleration (gal)	Max base shear (kN)
MLQT-4	70	2.045
	140	3.019
	200	4.000
	280	7.000
	400	7.909
	620	11.206
	800	13.825
	1000	15.207
	1240	16.556
	1400	17.021

When the LRB started working in the MLQT-2 specimen, the area of the hysteresis ring was approximately full [44]. The wall's carrying capacity remained stable after the LRB reached its maximum displacement. After the specimen reached the maximum load, the capacity of the wall decreased slowly, the displacement growth began to accelerate, the yield load of the hysteresis curve formed an inverse S shape, and the central part of the hysteresis curve grew fusiform.

The MLQT-3 hysteresis curve presented an inverse S trend in the negative direction (Figure 10) [45], which indicates that the shear deformation of the structure influenced the stiffness at the beginning of the load application process. This may be due to microcracks created inside the structure or slight relative displacement occurring at the junction. As the maximum acceleration reached 620 gal, the displacement continued to increase alongside a certain amount of plastic deformation. This formed a clear inverse S shape (Figure 10(d)) as the stiffness continued to degenerate.

As per the MLQT-4 hysteresis curve, as shown in Figure 11, the maximum lateral displacement of the model was within 6 mm when peak acceleration was 100 gal. Inputting a peak acceleration of 400 gal did not produce a sharp inverse S in the curve. The maximum displacement is

closer to four times greater than the 100 gal maximum displacement in the hysteretic curve, which suggests that the stiffness of the specimen degraded or the LRB deformed horizontally in the test [46]. From 620 gal to 1,000 gal, the shape of the hysteretic curve did not markedly change as the work of the LRB was stable [47]. The hysteresis ring area increased when the peak acceleration reached 1,024 gal; the LRB was damaged at this time and the sample reached its limit of seismic resistance.

3.3.2. Equivalent Horizontal Stiffness. Equivalent horizontal stiffness [48] is defined as a given component's resistance to deformation under pressure. It obtains per unit displacement of the force in the elastic range. The equivalent horizontal stiffness in the isolation layer can be calculated as follows:

$$K_h = \frac{(Q_1 - Q_2)}{(X_1 - X_2)}, \quad (38)$$

where K_h is the isolation layer's equivalent horizontal stiffness, Q_1 is the maximal shear force, Q_2 is the minimum shear force, X_1 is the maximum displacement, and X_2 is the minimum displacement.

The relationship between isolation layers with each LRB equivalent horizontal stiffness is expressed as

$$K_h = \sum K_j, \quad (39)$$

where K_j is each LRB's equivalent horizontal stiffness.

We determined each LRB's equivalent horizontal stiffness from MLQT-2, MLQT-3, and MLQT-4 for comparison against the design values. As shown in Figure 12, until the LRB was broken and the test was stopped, the LRB equivalent horizontal stiffness in MLQT-2 and MLQT-3 was higher than the LRB 250% equivalent shear strain stiffness. The equivalent horizontal stiffness of MLQT-2-4 did not exceed the maximum seismic resistance design value at any point [49]. Theoretically, stiffness should decrease linearly along the curve as the seismic wave strength increases. Our curve, however, shows an increase under a certain internal seismic strength in MLQT-2 and -3; growth points emerge along the seismic intensity generally corresponding to the LRB seismic resistance design. Abnormal changes in stiffness curves did not affect the LRB in achieving the expected target despite the theoretical inconsistencies.

We noted in our experiment that the lower connection plate of the LRB tended to separate from the rubber layer. This reduced the area of the connection between the rubber bottom and steel plate, causing a slight increase in vertical stress and slightly improving LRB horizontal stiffness. In MLQT-2 and MLQT-3, we found that the LRB components were broken due to the separation of the steel plate and rubber layer. The corresponding peak acceleration postyield stiffness and equivalent viscous damping ratio curve are further evidence of this phenomenon and further indicate that damage to the bearing affected the sample's mechanical properties. The LRB must be repaired properly after an "intense" earthquake occurs.

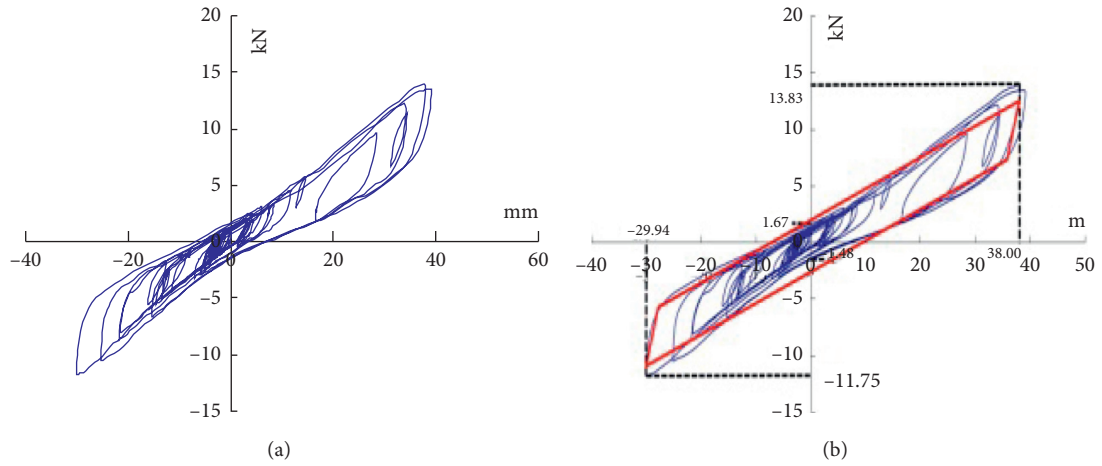


FIGURE 9: MLQT-4 (800 gal) hysteretic curve: (a) hysteresis curve of 90 mm LRB wall; (b) maximum hysteresis loop area.

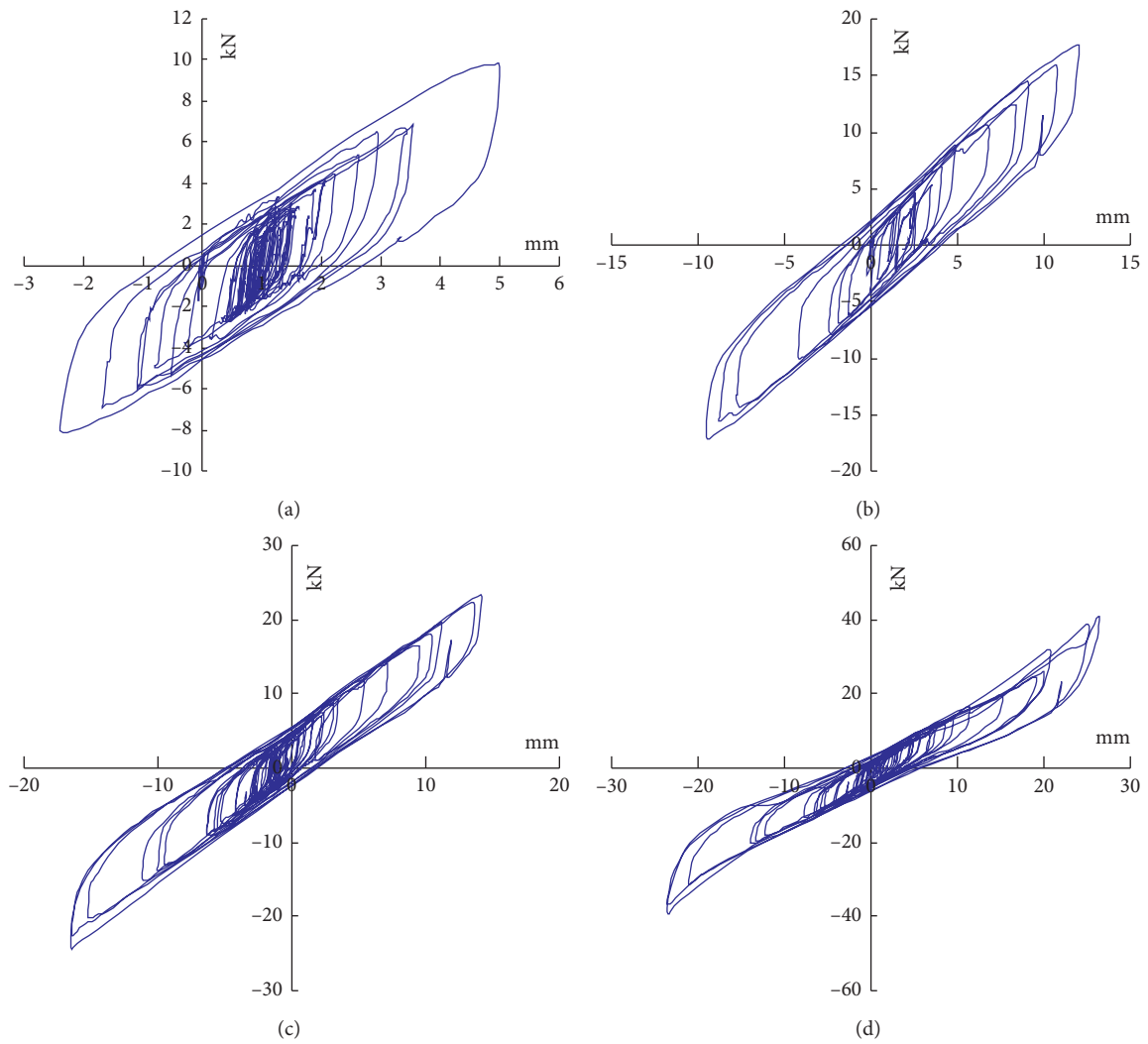


FIGURE 10: Specimens MLQT-3 hysteretic curve: (a) 100 gal; (b) 280 gal; (c) 400 gal; (d) 620 gal.

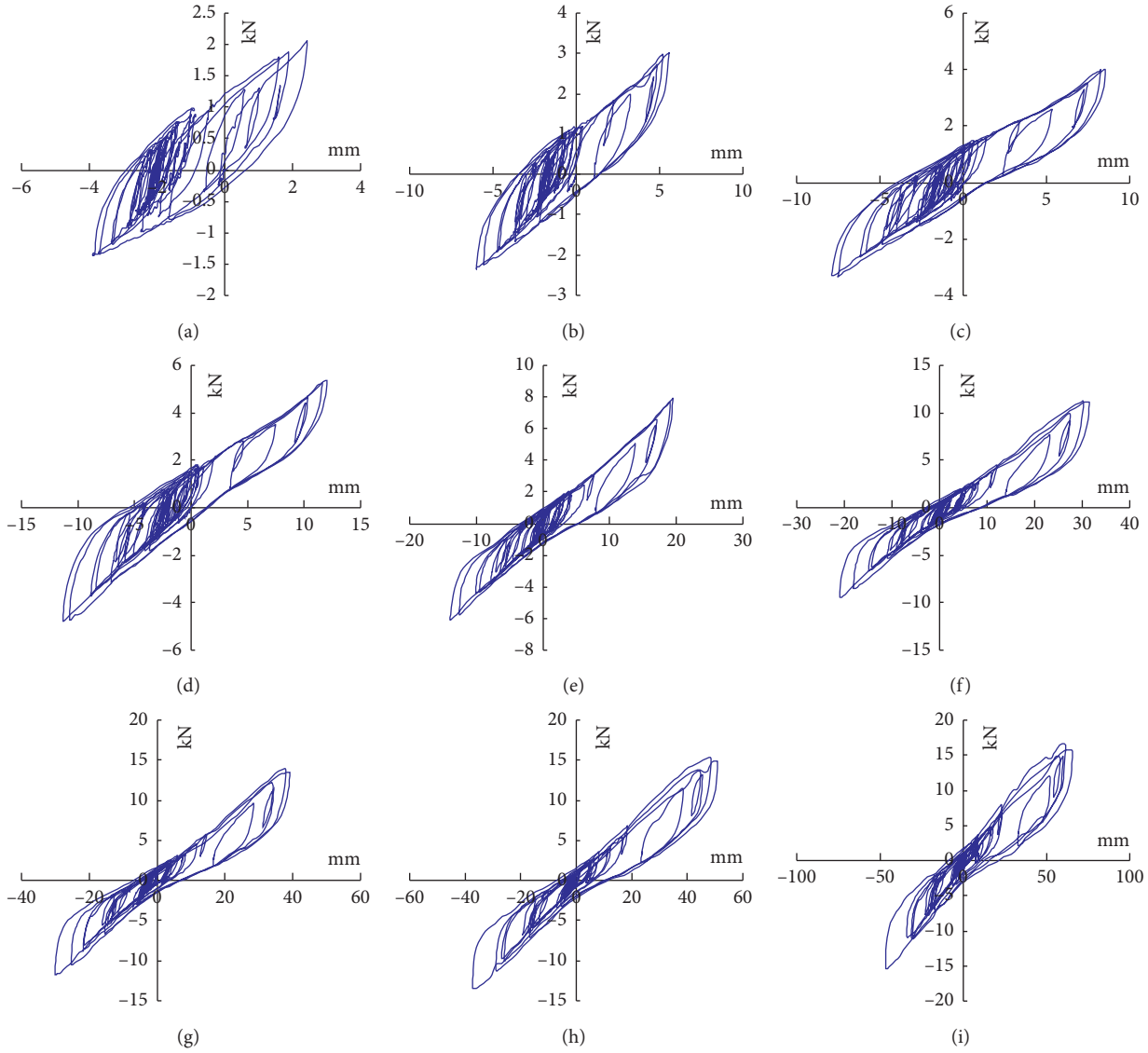


FIGURE 11: MLQT-4 hysteretic curve: (a) 70 gal; (b) 100 gal; (c) 200 gal; (d) 280 gal; (e) 400 gal; (f) 620 gal; (g) 800 gal; (h) 1000 gal; (i) 1240 gal.

3.3.3. *Postyield Stiffness.* We obtained hysteretic curves with different levels of simulated seismic intensity according to the experimental data. We then analyzed the LRB equivalent horizontal stiffness, postyield stiffness, and equivalent viscous damping ratio mechanical properties [50] to compare them against those measured in the LRB factory to test the applicability of the proposed method.

The postyield stiffness of the structural isolation layer is calculated as follows:

$$K_d = \left[\frac{(Q_{d1} - Q_1)/X_1 + (Q_{d2} - Q_2)/X_2}{2} \right], \quad (40)$$

where K_d is the postyield stiffness, Q_{d1} is the hysteretic curve positive direction intersecting with the shear axis, and Q_{d2} is the hysteretic curve negative direction intersecting with the shear axis.

We calculated the LRB postyield stiffness for MLQT-2-4 for comparison with the design values as shown in Figure 13.

The MLQT-4 postyield stiffness curve appears to be consistent with the relevant theory, as the elastic deformation range of the LRB is large. After the LRB yields, the stiffness rapidly increases where the contact area between the rubber layer and the connecting plate is stripped away. Compared to other LRB components, this is more obvious in the lower LRB (which has less rubber).

3.3.4. *Equivalent Viscous Damping Ratio.* The equivalent viscous damping ratio is a key parameter determining the equivalent period based on displacement in a seismic design [51]. The seismic isolation layer equivalent viscous damping ratio is calculated as follows:

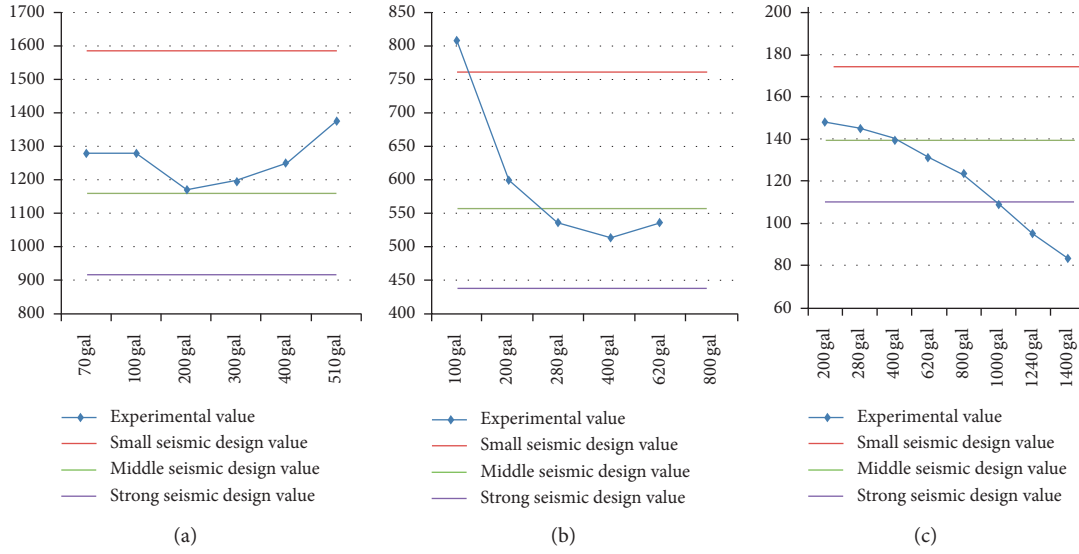


FIGURE 12: Equivalent horizontal stiffness: (a) MLQT-2; (b) MLQT-3; (c) MLQT-4.

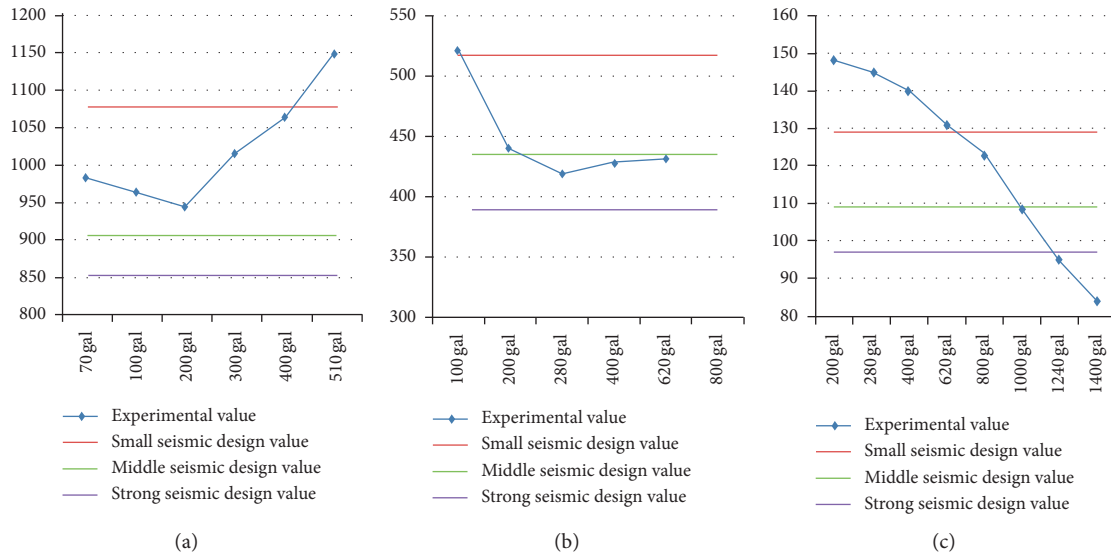


FIGURE 13: Postyield stiffness: (a) MLQT-2; (b) MLQT-3; (c) MLQT-4.

$$\zeta = \frac{2\Delta W}{\pi K_h (X_1 - X_2)^2}, \quad (41)$$

where ζ is the structural equivalent viscous damping ratio, ΔW is the envelope area of the hysteretic curve, and K_h is the structural isolation layer equivalent horizontal stiffness.

The equivalent viscous damping ratio of each LRB can be calculated as

$$\zeta = \sum \frac{K_j \zeta_j}{K_h}, \quad (42)$$

where ζ is the structural isolation layer equivalent viscous damping ratio, ζ_j represents each LRB's equivalent viscous damping ratio, K_h is the structural isolation layer equivalent

horizontal stiffness, and K_j represents each LRB's equivalent horizontal stiffness in the experiment.

Each LRB's equivalent viscous damping ratio was obtained from MLQT-2-4 and compared with the 250% LRB shear deformation horizontal property as shown in Figure 14.

As shown in Figure 14, the equivalent viscous damping ratios of MLQT-2-4 were not lower than the 250% horizontal deformation of each LRB at any point until the specimens were broken. The MLQT-2 curve fluctuated irregularly as earthquake intensity increased, which indicates that the elastic deformation range of the LRB is small. This may be related to its relatively low rubber content [52]. The MLQT-3 curve is more in line with the theoretical rationality of this design. The MLQT-4 curve begins to increase at

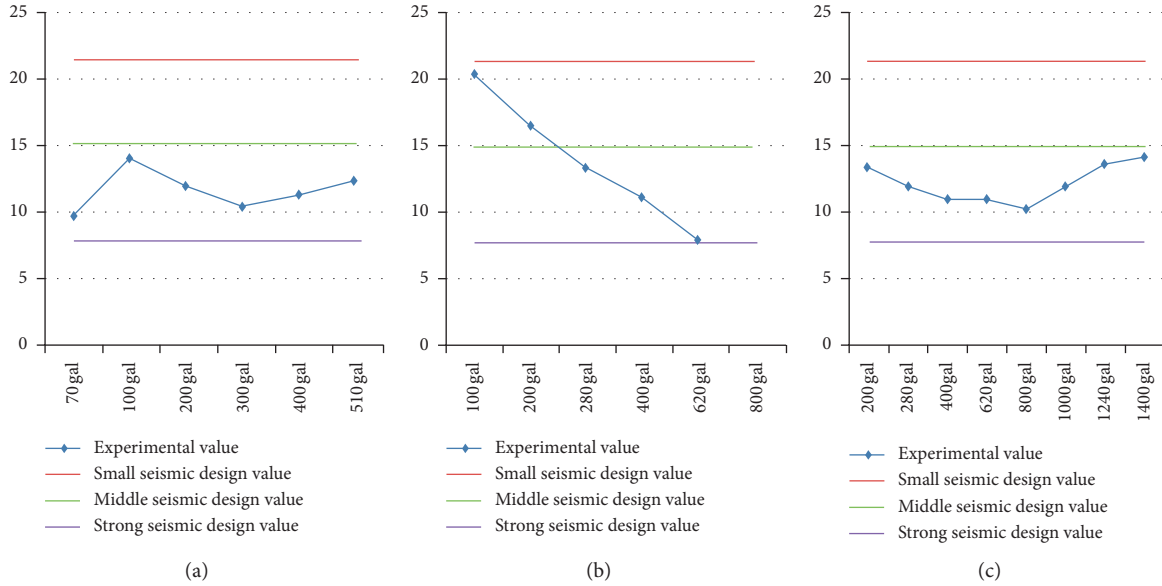


FIGURE 14: Equivalent viscous damping ratio: (a) MLQT-2; (b) MLQT-3; (c) MLQT-4.

620 cm/s², which is equivalent to 10 degrees of earthquake protection. The LRB was damaged under higher seismic intensity; it appears that a higher body coefficient renders higher seismic resistance.

4. LRB Experiment and Fitting Formula

4.1. Experiment Method. We conducted a horizontal stiffness experiment on five types of small LRB to explore various horizontal shearing strains and second shape coefficients as they affect the equivalent horizontal stiffness, yield stiffness, and hysteretic properties of the structure. We gave each shearing strain fitting formula an equivalent horizontal stiffness and yield stiffness while varying the second shape coefficient [2]. We analyzed the LRB horizontal stiffness related to the structure model seismic coefficient and horizontal displacement to create a curve-fitting formula. We used a small-diameter LRB to reflect the seismic effects on existing rural low masonry structures, as our goal was to gather results that may serve as a workable reference for bearing wall designs.

Residential buildings generally contain circle rubber bearings, the vertical stiffness and bearing capacity of which are related to the single rubber effective pressure area and free sides of the superficial area (first shape coefficient). Their stability is related to the inner rubber layer diameter divided by the total thickness of the inner rubber (second shape coefficient).

The LRB has the same steady vertical bearing capacity as other bearing components, in addition to favorable isolation, self-resetting, damping energy dissipation properties, and a large damping ratio ($\pm 25\%$). The LRB resilience model, which is commonly utilized in urban sky-rises, is a double linear model that has a much larger natural rubber bearing and high damping rubber bearing damping ratio; it is ineffective for rural dwelling isolation components. We used technical methods in this study to

decrease the LRB damping ratio and observe the isolation effects in small- and medium-intensity earthquakes. We focused on the horizontal property design indicators of postyield stiffness, yield force, equivalent stiffness, and equivalent damping ratio.

We adopted inverse calculation methods for our LRB designs and built the seismic response spectrum method into our parameter calculations [10]. The LRB lead core rod has about 7 MP yield stress with certain plastic deformation and repetitive loading properties. The original properties are restored upon the end of the deformation period. The LRB must be designed with sufficient horizontal stiffness to suit the opposite deformation between the foundation and new construction; the LRB can then absorb sufficient earthquake energy to remit seismic resistance to the structure.

$$W_e \gg E,$$

$$W_e = \frac{1}{2} Q_{\max} \delta_{\max}, \quad (43)$$

$$E = \frac{1}{2} M v_e^2.$$

The maximum shear coefficient can be calculated as follows:

$$\alpha = \frac{Q_{\max}}{Mg}, \quad (44)$$

$$Q_{\max} = K_H \delta_{\max},$$

and the mass, stiffness, and period relation is formulated here as

$$W_e = \frac{Mg^2 T^2 \alpha^2}{8\pi^2}, \quad (45)$$

where M is the total mass, g is the gravitational acceleration, K_H is the horizontal stiffness coefficient, and T is the natural period.

4.2. Horizontal Stiffness

4.2.1. Horizontal Stiffness Calculations. We obtained an LRB horizontal displacement-load-related curve from our experimental data adopting a sine wave of 0.5 Hz and shear strain of 100% third hysteresis. We calculated the experimental LRB equivalent horizontal stiffness K_h , equivalent damping ratio h_{eq} , and postyield stiffness K_d [6] as follows:

$$K_h = \frac{Q_1 - Q_2}{X_1 - X_2}, \quad (46)$$

$$h_{eq} = \frac{2\Delta W}{\pi K_h (X_1 - X_2)^2}, \quad (47)$$

$$K_d = \frac{1}{2} \left(\frac{Q_1 - Q_{d1}}{X_1} + \frac{Q_2 - Q_{d2}}{X_2} \right), \quad (48)$$

where Q_1 is the maximum shear force, Q_2 is the minimum shear force, X_1 is the maximum displacement, X_2 is the minimum displacement, Q_{d1} and Q_{d2} are the hysteresis curve positive and negative direction with the shear force coordinate as the crossing point, and ΔW is the hysteresis curve envelope size. The calculation results are listed in Table 2.

4.2.2. Effects on Shear Strain. We calculated the equivalent horizontal stiffness related to shear strain from the experimental LRB hysteresis curve as shown in Figure 15. The equivalent horizontal stiffness decreased as the shear strain increased in a nonlinear relation—a higher shear strain gave the LRB a better ability to withstand horizontal stiffness degeneration. The LRB equivalent horizontal stiffness affected shear strain when it was relatively low (e.g., $\gamma = 50\%$) and was stable when the shear strain was larger (e.g., $\gamma = 100\%$; $\gamma = 250\%$).

Figure 16 shows our experimental LRB postyield stiffness related to horizontal shear strain. In comparison to the effects on equivalent horizontal stiffness, the shear strain does not act strongly upon the postyield degenerate ability of the structure. The experimental LRB postyield decreased as the shear strain increased. When the shear strain was $\gamma = 100\%$ – $\gamma = 250\%$, the experimental LRB postyield change was confined to 15%.

4.2.3. Effects on Second Shape Coefficient. The second shape coefficient (S_2) is determined by dividing the respective experimental LRB layers' rubber diameters [7]. The fifth LRB in our setup has a different rubber shear elasticity modulus than the other four LRBs, so we only compared the first four LRBs' equivalent horizontal stiffness related to the S_2 curve (Figure 17). We found that the equivalent horizontal stiffness increased, as did the shear strain and increasing rate, as S_2 increased.

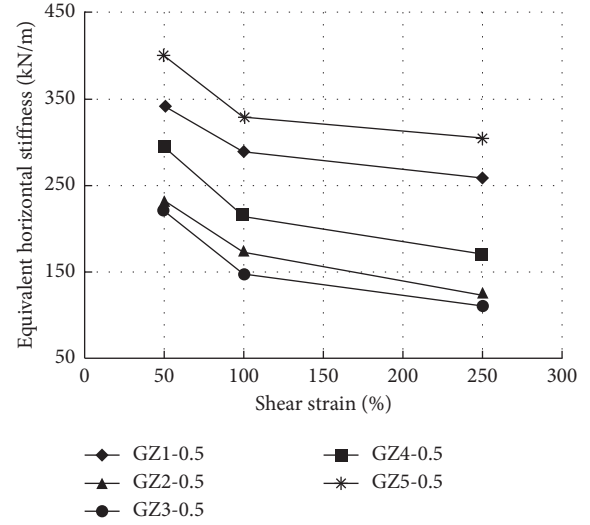


FIGURE 15: Relative equivalent horizontal stiffness with shear strain.

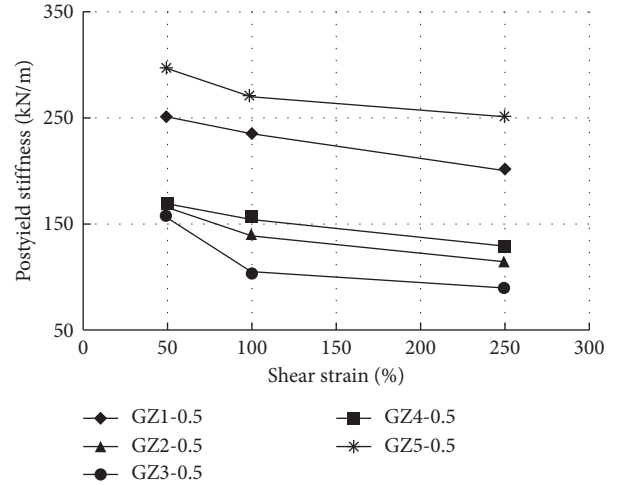


FIGURE 16: Relative postyield stiffness with shear strain.

Formulas (49)–(51) show where shear strains of 50%, 100%, and 250% change alongside the equivalent horizontal stiffness K_h with S_2 . The results of these formulas provide a workable reference for small-diameter LRB designs.

$$K_h(50\%) = 39.1S_2^2 - 267.4S_2 + 678.9 \quad (S_2 \leq 4.8), \quad (49)$$

$$K_h(100\%) = 34.9S_2^2 - 236.0S_2 + 560.3 \quad (S_2 \leq 4.8), \quad (50)$$

$$K_h(250\%) = 52.2S_2^2 - 374.7S_2 + 777.5 \quad (S_2 \leq 4.8). \quad (51)$$

As shown in Figure 17, when S_2 is 4.8, the equivalent horizontal stiffness-second shape coefficient curve slope mean value is 35.89; its maximum value does not exceed 63. When S_2 exceeds 4.8, the equivalent horizontal stiffness slope increases more steeply and the slope mean value is 226.22. The upper formula listed above is more accurate than the others in terms of the stable equivalent horizontal stiffness when S_2 is 4.8.

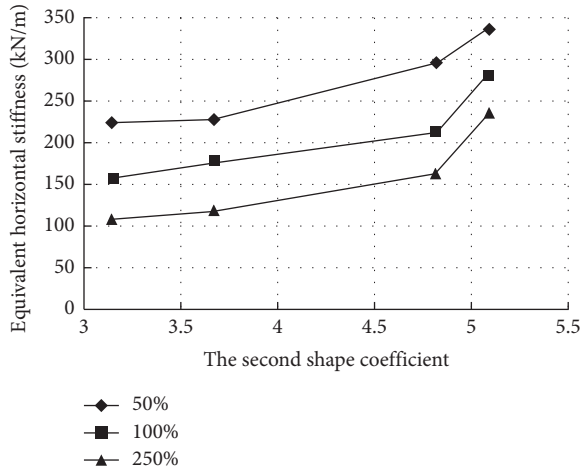


FIGURE 17: Relative equivalent horizontal stiffness with the second shape coefficient.

We also calculated the experimental LRB postyield stiffness K_d with the S_2 relative curve, as shown in Figure 18.

Under the same vertical pressure action, the postyield stiffness K_d increased as S_2 increased. At a certain S_2 , the K_d decreased and trended toward a constant value. The two relations can be described linearly using formulas (52)–(54). A higher S_2 can raise the LRB postyield stiffness within a certain range, but this effect is not obvious when S_2 exceeds 4.8. When selecting the LRB for use in rural masonry structures, restricting the second shape coefficient to 4.8 can ensure a safe structure while minimizing cost and reducing material waste.

$$K_d(50\%) = 21.1S_2 + 29.7 (S_2 \leq 4.8), \quad (52)$$

$$K_d(100\%) = 69.2S_2 + 112.6 (S_2 \leq 4.8), \quad (53)$$

$$K_d(250\%) = 48.3S_2 + 4.5 (S_2 \leq 4.8). \quad (54)$$

4.3. Analysis Progress. We next drew a pressure displacement-pressure curve to explore the vertical contraction stiffness after three loading cycles as shown in Table 9 [8]. We found that the supporter vertical stiffness discreteness increased over this curve, which indicates that the component's vertical pressure property is not stable.

Figure 4 shows the shear strain hysteretic loop at a frequency of 0.5 Hz.

As shown in Figure 4, the 1#–4# hysteretic loops are rhomboid and have straight lines along their sides. Component 5# was designed with a different rubber than the other four; its hysteretic loop is slightly bent in a positive direction. The 1# bearing hysteretic curve shear strain was 100% as shown in the third loop. The 0.1 Hz hysteretic loop areas for 1–5# are 115.98, 178.71, 222.59, 137.52, and 139.77, respectively. The 0.5 Hz hysteretic loop areas for 1–5# are 88.01, 175.2, 216.46, 134.46, and 122.7, respectively. The 0.1 Hz hysteretic loop area is larger than the others [53]. We drew its curve again for comparison as shown in Figure 19 to

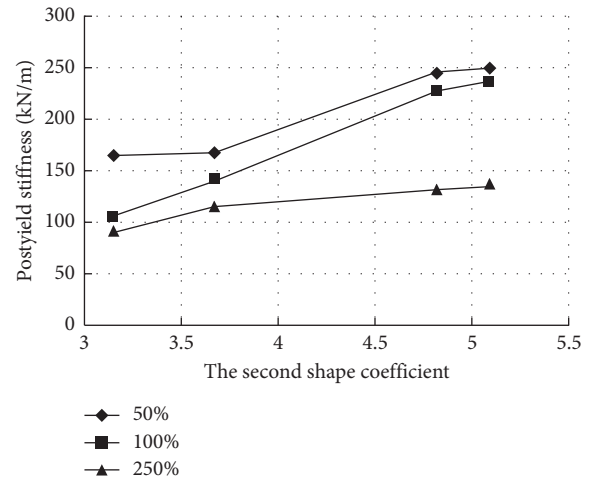


FIGURE 18: Postyield stiffness related to the second shape coefficient.

explore the relatively stable changes in the LRB load-displacement curve at higher loading frequency.

We separately input a 0.5 Hz sine wave to the five experimental LRB components and imposed maximum displacement loading of 50%, 100%, and 250%. There was no apparent difference among the LRBs in this case, so we redrew the LRB GZD-0.5 hysteretic curve for comparison as shown in Figure 20.

When the shear strain was 50% or 100%, the LRB hysteretic curves were rhomboid and every loop could be divided into four stages according to the loading process. We observed linear regularity among the horizontal loading and displacement indicators in this case. When the shear strain was 250%, the hysteretic curve formed an inverse S in a positive direction. The LRB stiffness degenerated to a certain extent as the inner rubber of the bearing slid along the steel plate. The area of the hysteretic curve increased as the shear strain increased, as the supporter degraded the energy resistance.

4.4. Effect of Supporter Stiffness on Isolation

4.4.1. Model Design. The LRB isolation effects can be balanced according to the horizontal seismic coefficient and horizontal displacement. Seismic fortification intensity is generally 6–8 degrees (0.20 g); in rural areas, the horizontal seismic coefficient should be less than 0.4. The isolation structure's horizontal displacement should be less than 0.55 times the bearing's effective diameter or 3-fold greater than the inner rubber's total thickness [54]. For the purposes of our experiment, we set the LRB horizontal displacement to an effective diameter of 0.55 multiplied by 60.5 mm.

We used a typical rural masonry dwelling to design our finite element calculation model and shaking table test model. The model is a two-layer single-bay brick masonry house with a reduced-scale (1:2) size of 2.25 m × 1.95 m × 3.3 m and a wall thickness of 120 mm. The four corners of the "house" were given four identical LRBs. The door was a one-layer 450 mm

TABLE 9: Pressure stiffness K_v calculation results.

Bearing	1 [#]		2 [#]		3 [#]		4 [#]		5 [#]	
Number vertical	1-1	1-2	2-1	2-2	3-1	3-2	4-1	4-2	5-1	5-2
Stiffness K_v (kN/mm)	47.91	57.22	42.04	42.04	29.86	29.01	38.87	36.79	62.42	71.03

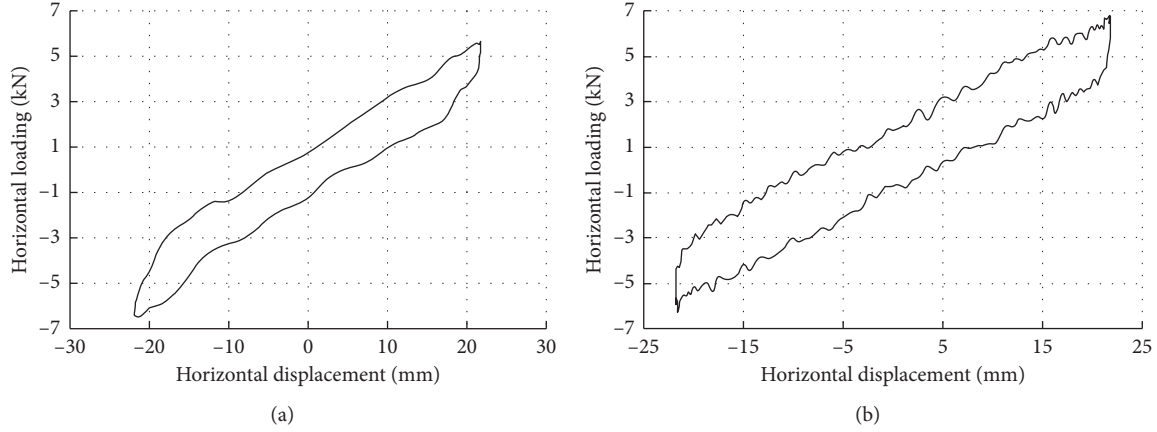


FIGURE 19: 1# bearing third hysteretic loop comparison: (a) 0.5 Hz loading frequency; (b) 0.1 Hz loading frequency.

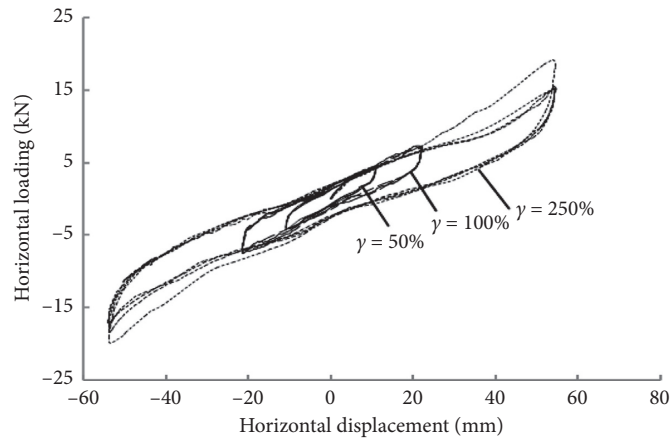


FIGURE 20: GZ5-0.5 hysteretic curves with varying shear strain.

wide opening with sliding supporters (LRBs) on either side; the upper part of the slider was connected to the structure while the lower part slid freely along the pedestal plane.

We used finite element software SAP2000 to construct the isolated structure model. LRBs 1–4# were, respectively, imposed as model supporters and El Centro waves were input separately in X and Y directions. The peak acceleration was 8.5 degrees and adjusted to 300 gal. We used the model to calculate the structure's horizontal seismic coefficient and maximum horizontal displacement.

4.4.2. Rural Building Isolated Parameter Estimation. We analyzed the above model's horizontal seismic coefficient and maximum horizontal displacement to determine the experimental LRB postyield stiffness and equivalent horizontal stiffness, as shown in Figures 21–24.

The model seismic coefficient showed an increasing and nearly linear trend with LRB postyield addition. The coefficients were similar in X and Y directions when the supporter postyield stiffness was relatively small; the difference between them increased as this stiffness increased.

Formulas (46) and (47) are the X - and Y -direction seismic coefficient (β_x, β_y)-postyield stiffness (K_d) relations, respectively.

$$\begin{aligned}\beta_x &= 1.6 \times 10^{-3} K_d + 0.122, \\ \beta_y &= 8.6 \times 10^{-4} K_d + 0.178.\end{aligned}\quad (55)$$

The model horizontal displacement decreased as the supporter postyield stiffness increased in a nearly linear relation [55]. The differences in X - and Y -direction horizontal displacement were within 3 mm, which suggests that

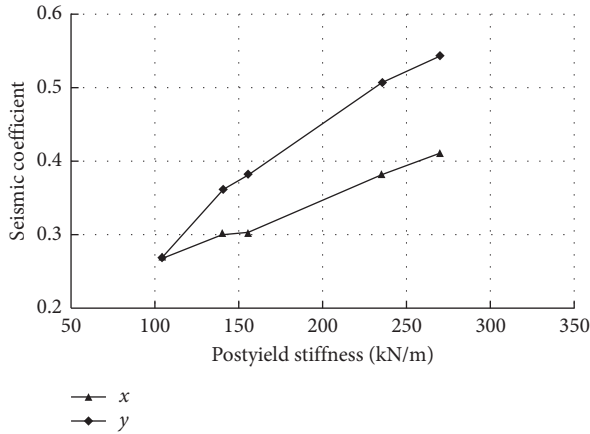


FIGURE 21: Seismic coefficient related to postyield stiffness.

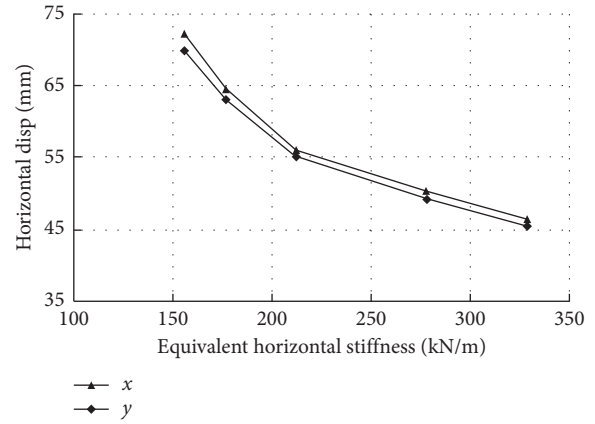


FIGURE 24: Horizontal displacement related to equivalent horizontal stiffness.

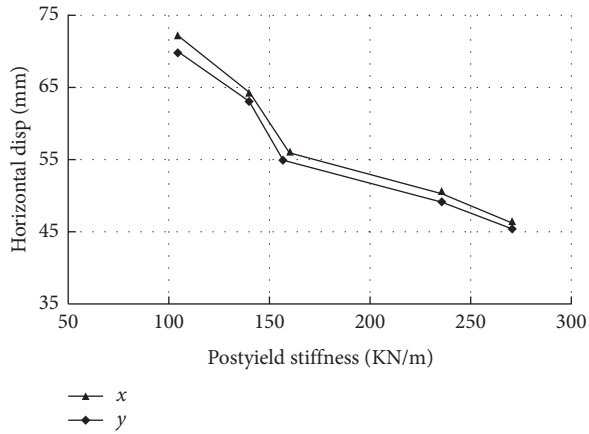


FIGURE 22: Horizontal displacement related to postyield stiffness.

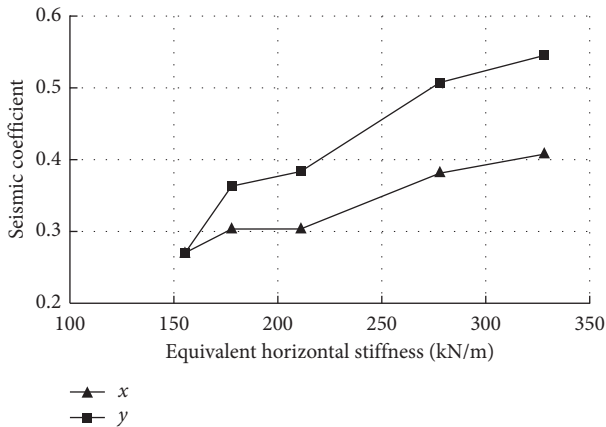


FIGURE 23: Seismic coefficient related to equivalent horizontal stiffness.

postyield stiffness does not affect the disparity between positive and negative displacement values. We established formula (56) as a reference for selecting the largest and safest possible displacement value according to the horizontal displacement (u)-postyield stiffness (K_d) curve:

$$u = -0.147K_d + 84.709. \quad (56)$$

As shown in Figures 21–24, the model seismic coefficient and horizontal displacement change regularly with equivalent horizontal stiffness. Both indicators showed similar postyield relations, but neither are linear. We fitted the curve to write a formula for the XY direction seismic coefficient (β_x, β_y)-equivalent horizontal stiffness (K_h) relation (formulas (57) and (58)). The horizontal displacement (μ)-equivalent horizontal stiffness (K_h) relative curve, which contains a quadratic function, is arguably more accurate; the X-direction is fitted in this case by formula (59).

$$\beta_x = 8.1 \times 10^{-4}K_h + 0.147, \quad (57)$$

$$\beta_y = 1.51 \times 10^{-3}K_h + 0.065, \quad (58)$$

$$\mu = 9.1 \times 10^{-4}K_h^2 - 0.583k_h + 139.87. \quad (59)$$

LRB postyield stiffness should be 149.7–167.8 N/mm and equivalent horizontal stiffness should be 193.9–218.65 N/mm when the horizontal displacement is less than 60.5 mm and the seismic coefficient is below 0.4 requirements, so we selected the 4# LRB accordingly to conduct our shaking table test.

4.4.3. Seismic Coefficient. The isolated masonry structure horizontal seismic coefficient can be determined by multi-storey masonry calculation. A smaller seismic coefficient indicates stronger seismic resistance but also generally reflects greater horizontal displacement in the LRB. The horizontal displacement thus must be restricted within a certain value; in this case, the isolation structure’s horizontal seismic coefficient should be less than 0.4.

We constructed a test bearing based on actual rural dwelling design and material requirements and then subjected it to a shaking table test. After inputting an 8.5 degree (300 gal peak acceleration) El Centro wave, we observed the deformation concentration in the isolation layer; the upper structure was altered but did not present any apparent

TABLE 10: LRB base displacement and seismic coefficient results.

Supporter number	Base displacement (mm)	Seismic coefficient
1 [#]	50.412	0.507
2 [#]	72.261	0.265
3 [#]	64.6	0.382
4 [#]	56.11	0.373
5 [#]	44.227	0.544

cracks. When the seismic wave peak acceleration reached 800 gal, the structure remained intact and its maximum horizontal displacement value was permissible. To this effect, the proposed LRB is safe and feasible.

In an earthquake, the isolation layer presents horizontal displacement which creates a displacement in the upper structure. The seismic structure's top storey may show greater displacement under certain earthquake conditions even when the isolation layer's displacement is relatively small. The support will be destroyed when the isolation layer's horizontal displacement exceeds the LRB limit; in this case, the entire upper structure may fail. We assert that support displacement should not exceed a minimum effective diameter of 0.55- or 3-fold greater than the inner rubber's total thickness. The effective LRB diameters in this experiment were 110 mm, in which case the horizontal displacement limit is 60.5 mm.

We simulated an earthquake wave acting on this model in SAP2000. Again, five LRBs were modeled with 8.5 fortification intensity and a 0.3 g structure base displacement average value. As shown in Table 10, only the 4[#] LRB satisfied both base displacement less than 60.5 mm and seismic coefficient less than 0.4.

5. Conclusions

We conducted an experiment to test the seismic performance and mechanical failure of several LRB structural specimens in this study, each with different parameters and excited by seismic waves of varying intensity. Our conclusions can be summarized as follows.

- (1) The 50 mm thick LRB specimen MLQT-2 was ineffective as its rubber layer is too thin (3×1.2 mm). The 57 mm thick LRB specimen MLQT-3 LRB exceeds the limit displacement for strong-intensity seismic waves. LRB specimen MLQT-4, which is 90 mm thick, can withstand middle-intensity seismic waves. The LRB exceeds the limit displacement for strong-intensity seismic waves in this case, but the LRB and structure were unbroken by the end of the test (though any stronger seismic waves would cause the LRB to break)
- (2) MLQT-4 was shown to withstand stronger peak acceleration seismic waves than other specimens due to its effective masonry performance and mortar strength. Changes in LRB thickness changes do not appear to affect bearing capacity but do change the position of the centroid. We recommend that the superstructure be designed according to extant standards and that the sliding bearing isolator

support be placed in the appropriate position according to the stresses acting on the structure

- (3) We wrote a seismic coefficient fitting formula that reflects the regular changes in small-diameter LRB horizontal displacement according to our shaking table test results. This formula may serve as a workable reference for practical LRB designs
- (4) The structure's horizontal seismic coefficient and horizontal displacement have a fittable relation with the LRB's horizontal stiffness (provided that said stiffness falls within a reasonable range in the shaking table test)
- (5) Various shear strains produce different forms of LRB equivalent horizontal stiffness and postyield indicators according to the second shape coefficient. When this coefficient is less than 4.8, the LRB equivalent horizontal stiffness changes in a stable manner and the curve of the two indicators can be accurately fitted. Restricting the second shape coefficient below 4.8 can assist in reducing the cost and material waste of the structure's fabrication
- (6) We analyzed the LRB horizontal stiffness with the structure model seismic coefficient and horizontal displacement relation to establish a curve-fitting formula. We input our shaking table test results to find that a small-diameter LRB remits ideal seismic resistance in typical, rural low masonry structures

Data Availability

The raw/processed data required to reproduce these findings cannot be shared at this time, as they are also being utilized in an ongoing study.

Disclosure

The work described in this article is part of the author's own Ph.D. academic dissertation, "Low isolated masonry structures antiseismic property experimental study and its application."

Conflicts of Interest

The author declares no conflicts of interest.

Acknowledgments

This work was funded by the Twelve Five National Science Supporting Plan Foundation of China (Grant no. 2014BAL06B04).

References

- [1] B. Erkus and E. A. Johnson, "A control design methodology for the benchmark base isolated building with bilinear isolation," in *Proceedings of the Structures Congress 2004*, p. 8, May 2014.

- [2] M. Mcvay, D. Bloomquist, D. Vanderlinde et al., "Centrifuge modeling of laterally loaded pile groups in sands," *ASTM Geotechnical Testing Journal*, vol. 17, no. 2, pp. 129–137, 1994.
- [3] A. N. Gent, "Elastic stability of rubber compression springs," *Journal of Mechanical Engineering Science*, vol. 6, no. 4, pp. 318–326, 1964.
- [4] C. G. Koh and J. M. Kelly, "A simple mechanical model for electrometric bearing used in base isolation," *Journal of Engineering Mechanics*, vol. 30, no. 12, pp. 933–943, 1998.
- [5] J. Kelly and M. R. Marsico, "Stability and post-buckling behavior in nonbolted elastomeric isolators," *Seismic Isolation and Protective Systems*, vol. 1, no. 1, pp. 41–54, 2010.
- [6] S. Nagarajaiah, A. M. Reinhorn, and M. C. Constantinou, "Nonlinear dynamic analysis of 3-D-base-isolated structures," *Journal of Structural Engineering*, vol. 117, no. 7, pp. 2035–2054, 1991.
- [7] M. Reinhorn, S. Nagarajaiah, M. C. Constantinou et al., *Nonlinear Dynamic Analysis of Three-Dimensional Base Structures (3DBASIS-TABS)*, National Center For Earthquake Research, State University of New York at Buffalo, Buffalo, NY, USA, 1994.
- [8] J. M. Kelly, *Earthquake-Resistant Design with Rubber*, Springer-Verlag, London, UK, 1997.
- [9] S.T. Sinkhole, "Damage to masonry structure," *Journal of Performance of Constructed Facilities*, vol. 7, no. 1, pp. 67–72, 2009.
- [10] H. C. Uzoegbo, J. V. Ngowi, and R. Senthivel, "Concrete repair, rehabilitation and retrofitting," in *Proceedings of the International Conference on Concrete Repair, Rehabilitation and Retrofitting, ICCRRR 2005*, pp. 429-430, Cape Town, South Africa, November 2005.
- [11] C. R. Willis, Q. Yang, R. Seracino, and M. C. Griffith, "Damaged masonry walls in two-way bending retrofitted with vertical FRP strips," *Construction and Building Materials*, vol. 23, no. 4, pp. 1591–1604, 2009.
- [12] A. Elvin, "Experimentally applied earthquakes and associated loading on a full-scale dry-stacked masonry structure," *Journal of the South African Institution of Civil Engineering*, vol. 51, no. 1, pp. 15–25, 2009.
- [13] A. Amorosi, D. Boldini, G. de Felice, and M. Malena, "Tunnelling-induced deformation on a masonry structure: a numerical approach. Geotechnical aspects of underground construction in soft ground," in *Proceedings of the 7th International Symposium on Geotechnical Aspects of Underground Construction in Soft Ground*, pp. 353–359, Rome, Italy, May 2012.
- [14] S. P. Schneider and C. W. Roeder, "An inelastic substructure technique for the pseudodynamic test method," *Earthquake Engineering & Structural Dynamics*, vol. 23, no. 7, pp. 761–775, 1994.
- [15] D. Isobe and M. Tsuda, "Seismic collapse analysis of reinforced concrete framed structures using the finite element method," *Earthquake Engineering and Structural Dynamics*, vol. 32, no. 13, pp. 1051–1103, 2003.
- [16] M. Bruneau, "State-of-the-art report on the seismic performance of unreinforced masonry building," *Journal of Structural Engineering (ASCE)*, vol. 120, no. 1, p. 4, 1994.
- [17] A. Das, S. Kanti, and A. Dutta, "Shaking table testing of unreinforced brick masonry building test model isolated by U-FREI," *Earthquake Engineering & Structural Dynamics*, vol. 61, pp. 43–45, 2015.
- [18] L. Soveja and M. Budecu, "Analysis and design of a base isolation system for an old church with masonry structure," *Intersections*, vol. 13, no. 2, pp. 3–8, 2016.
- [19] A. Chourasia, S. K. Bhattachayya, N. M. Bhandari, and P. Bhargava, "Seismic performance of different masonry building: full-scale experiment study," *Journal of Performance of Constructed Facilities*, vol. 30, no. 5, 2016.
- [20] L. Salvatori, A. M. Marra, G. Bartoli, and P. Spinelli, "Probabilistic seismic performance of masonry towers: general procedure and a simplified implementation," *Engineering Structures*, vol. 94, pp. 82–95, 2015.
- [21] F. D. Scheaua, "Description of a composed seismic isolation system for bridge structures," *Analele Universității Eftimie Murgu*, vol. 43, pp. 357–362, 2015.
- [22] A. H. Baziar, M. Safi, and L. Shahriari, "Evaluation of seismic behavior of masonry building materials by using a plastic failure model," *Islamic Azad University*, vol. 3, pp. 41–55, 2011.
- [23] D. Foti, M. Debernardis, and V. Paparella, "Structural safety control of masonry building: non-linear static analysis with a non-linear shear strength criterion," in *Proceedings of the Eleventh International Conference on Computational Structures Technology*, Dubrovnik, Croatia, September 2012.
- [24] P. Tsopelas, M. C. Constantinou, Y. S. Kim, and S. Okamoto, "Experimental study of FPS system in bridge seismic isolation," *Earthquake Engineering and Structural Dynamics*, vol. 25, pp. 65–78, 2014.
- [25] P. Tan, K. Xu, B. Wang, and F. Zhou, "Performance study of isolated rural buildings using novel simple isolators," *Tumu Gongcheng Xuebao/China Civil Engineering Journal*, vol. 46, no. 5, pp. 64–70, 2013.
- [26] Q. Ali, A. Naeem, N. Ahmad, and B. Alam, "In-situ dynamic testing of masonry structure by means of underground explosions simulating earthquake motions, a unique case study," *International Journal of Earth Sciences and Engineering*, vol. 5, no. 5, pp. 1196–1207, 2012.
- [27] P. B. Shing, M. T. Vannan, and E. Cater, "Implicit time integration for pseudodynamic tests," *Earthquake Engineering and Structural Dynamics*, vol. 20, pp. 515–576, 1991.
- [28] D. M. Lee, "Base isolation for torsion reduction in asymmetric structures under earthquake loading," *Earthquake Engineering and Structural Dynamics*, vol. 112, no. 8, pp. 349–359, 1980.
- [29] D. Benedetti, P. Carydis, and P. Pezzoli, "Study for reinforcement planning of masonry structure with cracks at Bayon main tower, Angkor," in *Proceedings of the 10th International Conference on Advance in Discontinuous Numerical Methods and Application in Geomechanics and Geoengineering, ICADD 10*, pp. 147–149, Honolulu, HI, USA, December 2011.
- [30] E. Jampole, S. Eeri, G. Deierlein et al., "Full scale dynamic testing of a sliding seismically isolated unibody house," *Earthquake Spectra*, vol. 32, no. 4, Article ID 2245, 2016.
- [31] G. Pan, L. Dong, and Y. Xiao, "Simulation and experiment study on six-degrees-of-freedom active micro-vibration isolation platform," *Modeling Simulation and Optimization Technologies and Applications*, vol. 58, pp. 130–134, 2016.
- [32] C. Modena, G. Zanardo, and D. Zonta, "Seismic response of reinforced masonry structures," vol. 9, pp. 90–91, 2016.
- [33] C. Mordant, M. Dietz, C. Taylor et al., "Shaking table tests on unreinforced load-bearing masonry frames," in *Proceedings of the 9th International Conference on Structural Dynamics*, pp. 229–236, Porto, Portugal, June 2014.
- [34] H. Gavin, C. Alhan, and N. Oka, "Fault tolerance of semi-active seismic isolation," *Journal of Structural Engineering*, pp. 1–16, 2001.

- [35] H. G. Kim, S. Yoshitomi, T. Masaaki, and I. Takewaki, "Post-tensioning high-hardness rubber damper system for vibration control of residential houses and building structures," *Advances in Structural Engineering*, vol. 15, no. 12, pp. 2157–2172, 2012.
- [36] M. Betti, L. Galano, and A. Vignoli, "Comparative analysis on the seismic behaviour of unreinforced masonry buildings with flexible diaphragms," *Engineering Structures*, vol. 61, pp. 195–208, 2014.
- [37] S. Jia, Y. Liu, W. Cao, W. Ye, and Y. Zhang, "Experimental study on the force-bearing performance of masonry structures with a marble-graphite slide seismic isolator at the foundation," *Applied Sciences*, vol. 6, no. 11, pp. 345–364, 2016.
- [38] F. M. Mazzolani, A. Mandara, and G. Laezza, "Design criteria for the use of special devices in the seismic protection of masonry structures," in *Proceedings of the 8th World Seminar on Seismic Isolation, Energy Dissipation and Active Vibration Control of Structures*, pp. 6–10, Yerevan, Armenia, October 2003.
- [39] B. Peng, X. L. Gu, and Y. L. Qian, "Parameter study on computer simulation of collapse responses for masonry structures," in *Proceedings of the 13th International Brick and Block Masonry Conference*, Amsterdam, Netherlands, July 2004.
- [40] J. Coene, S. Francois, and G. Degrande, "Non-linear static analysis of masonry structures," in *Proceedings of the XIII International Conference on Computational Plasticity*, pp. 1053–1064, Barcelona, Spain, September 2015.
- [41] L. S. Wei, F. L. Zhou, P. Tan, and M. Ren, "Research and application on three-dimensional seismic and vibration isolation for building," *Journal of Harbin Institute of Technology*, vol. 18, no. 1, pp. 62–66, 2011.
- [42] M. A. Claudia and H. Xing, "Experimental investigation on the seismic performance of a service vibration isolation platform for protection of equipment," in *Proceedings of the Structures Congress*, pp. 1774–1785, Portland, Oregon, April 2015.
- [43] I. N. Doudoumis, F. Gravalas, and N. I. Doudoumis, "Analytical modeling of elastomeric lead-rubber bearings with the use of finite element micro models," in *Proceedings of the 5th GRACM International congress Computational Mechanics*, Limassol, Cyprus, June 2005.
- [44] R. Popescu and G. Popescu, "Modern design method for structural analysis of masonry buildings in seismic areas," in *Proceedings of the 14th World Conference on Earthquake Engineering*, Beijing, China, October 2008.
- [45] P. R. Nanda, P. Agarwal, and M. Shrikhande, "Base isolation system for masonry buildings," *Asian Journal of Civil Engineering*, vol. 13, no. 2, pp. 195–202, 2012.
- [46] N. Mendes and P. B. Lourenco, "Seismic vulnerability of existing masonry building: nonlinear parametric analysis," *Seismic Assessment Behavior and Retrofit of Heritage Building and Monument*, pp. 139–164, Springer International Publishing, New York City, NY, USA, 2015.
- [47] S. Bandyopadhyay, A. Sengupta, and G. R. Reddy, "Performance of sand and shredded rubber tire mixture as a natural base isolator for earthquake protection," *Earthquake Engineering and Engineering Vibration*, vol. 14, no. 4, pp. 683–693, 2015.
- [48] Z. T. Rakicevic, A. Bogdanovic, D. Jurukovski, and P. Nawrotzki, "Effectiveness of tune mass damper in the reduction of the seismic response of the structure," *Bulletin of Earthquake Engineering*, vol. 10, no. 3, Article ID 1073, 2012.
- [49] H. Toopchi-Nezhad, M. J. Tait, and R. G. Drysdale, "Effects of bearing geometry on base isolation characteristics for masonry structures," in *Proceedings of the 11th Canadian Masonry Symposium*, Toronto, ON, USA, May 2009.
- [50] D. An, T. J. Qu, and J. W. Liang, "Full-scale test on seismic performance of masonry structure," *Applied Mechanics and Materials*, vol. 204–208, pp. 2610–2617, 2012.
- [51] A. Elvin and H. C. Uzoegbo, "Response of a full-scale dry-stack masonry structure subject to experimentally applied earthquake loading," *Journal of the South African Institution of Civil Engineering*, vol. 53, no. 1, pp. 22–32, 2011.
- [52] M. R. Marsico, "Stability and post-buckling behavior in nonbolted elastometric isolators," *Seismic Isolation and Protective*, vol. 1, no. 1, pp. 41–44, 2010.
- [53] C. G. Koh and J. M. Kelly, "A simple mechanical model for electrometric bearing used in base isolation," *Journal of Engineering Mechanics*, vol. 30, no. 12, pp. 931–932, 2016.
- [54] F. Natario, "Analysis of masonry structures with damage models," *M.Sc. thesis*, pp. 10–31, Técnico Lisboa, Lisboa, Portugal, 2006.
- [55] A. Drougkas, P. Roca, and C. Molins, "Numerical prediction of the behavior, strength and elasticity of masonry in compression," *Engineering Structures*, vol. 90, pp. 15–28, 2015.